On the Role of the Meridional Jet and Horizontal Potential Vorticity Dipole in the Iowa Derecho of 10 August 2020

MATTHEW H. HITCHMAN[a] AND SHELLIE M. ROWE[a]

[a] *Department of Atmospheric and Oceanic Sciences, University of Wisconsin–Madison, Madison, Wisconsin*

(Manuscript received 3 August 2023, in final form 2 April 2024, accepted 17 April 2024)

ABSTRACT: On 10 August 2020, a derecho caused widespread damage across Iowa and Illinois. Des Moines station data show that the arrival of the gust front was characterized by an abrupt shift to northerly flow, exceeding 22 m s^{-1} for ~20 min. To test the hypothesis that this northerly jet is associated with a horizontal potential vorticity (PV) dipole in the lower troposphere, we investigated the structure of PV in the University of Wisconsin Nonhydrostatic Modeling System (UWNMS) and of absolute vorticity in High-Resolution Rapid Refresh (HRRR) forecast analyses. This structure is described here for the first time. The negative PV member coincides with the downdraft, while the positive PV member coincides with the updraft, with a northerly jet between. The westerly inflow jet descends anticyclonically in the downdraft, joining with northerly flow from the surface anticyclone. The resulting northerly outflow jet creates the trailing comma-shaped radar echo. The speed of propagation of the derecho is similar to the westerly wind maximum in the 3–5-km layer associated with the approaching synoptic cyclone, which acts as a steering level for resonant amplification. Idealized diagrams and 3D isosurfaces illustrate the commonality of the PV dipole/northerly jet structure. Differences in this structure among the three model states are related to low-level wind shear theory. The PV dipole coincides with the pattern of diabatic stretching tendency, which shifts westward and downward relative to the updraft/downdraft with increasing tilt. The PV dipole can contribute toward dynamical stability in a derecho.

SIGNIFICANCE STATEMENT: The purpose of this work is to investigate the structure of potential vorticity (PV) in the lower troposphere in a derecho. It is found that a northerly outflow jet occurs between an east–west-oriented horizontal PV dipole, which is described here for the first time. The negative PV member coincides with the downdraft and is inertially unstable, while the positive PV member coincides with the updraft. This work contributes toward the theory of resonant structures and longevity. The 3–5-km westerly inflow layer constitutes a steering level, which controls propagation speed despite differences in structure. The degree of westward tilt with height is related to the pattern of forcing by diabatic stretching in producing the PV dipole.

KEYWORDS: Convective storms/systems; Mesoscale systems; Potential vorticity; Updrafts/downdrafts; Derecho; Model comparison

1. Introduction

Deep convective updrafts and downdrafts play a crucial role in determining the growth and structure of mesoscale convective systems (MCSs). Davies-Jones (1984), Montgomery et al. (2006), Chagnon and Gray (2009), Davis and Galarneau (2009), and others have shown that a horizontal potential vorticity (PV) dipole can be formed by an updraft in shear, where horizontally oriented vorticity can be bent into a horseshoe shape by an updraft caused by diabatic heating. Hitchman and Rowe (2017, 2019) studied horizontal PV dipoles in the upper troposphere/lower stratosphere (UTLS) over deep convection in tropical and midlatitude cyclones and found amplitudes of ~±10–20 PVU (1 PVU = 10^{-6} K kg^{-1} m^2 s^{-1}). They suggested that UTLS PV dipole formation by the diabatic tilting term can be interpreted in terms of momentum transport by an updraft in shear. Air transported into an environment moving at a different speed and direction will create a mesoscale jet and therefore an associated horizontal PV dipole. Since vertical motion is limited by both the ground and the discontinuity in static stability at the tropopause, it was hypothesized that a downdraft in shear might create a mesoscale jet and horizontal PV dipole in the lower troposphere. Since a downdraft in shear is an essential aspect of a derecho, it was decided to investigate the PV structure of a derecho in the lower troposphere.

It is of interest to study PV dipoles since they can have a longer lifetime than the convection that initiates them (Chagnon and Gray 2009; Weijenborg et al. 2017). The emanation of gravity wave activity has been shown to occur simultaneously with the creation of horizontal vortex dipoles (e.g., Snyder et al. 2007, 2009; Muraki and Snyder 2007; Wang et al. 2009; Hernandez-Duenas et al. 2014; Plougonven and Zhang 2014; Rocha et al. 2018). The formation of horizontal PV dipoles and the emission of gravity waves can play a significant role in the dynamical adjustment process by which a derecho evolves into a balanced structure.

The derecho is a particularly damaging and long-lasting type of MCS, with a characteristic westerly inflow layer and downdraft. Corfidi et al. (2016) define a derecho as "a family

Supplemental information related to this paper is available at the Journals Online website: https://doi.org/10.1175/MWR-D-23-0168.s1.

Corresponding author: Shellie M. Rowe, rowe1@wisc.edu

DOI: 10.1175/MWR-D-23-0168.1

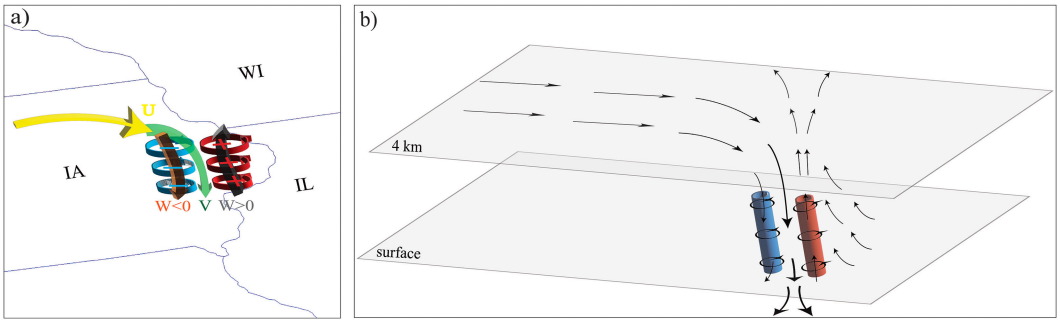

FIG. 1. Idealized 3D representation in the lower troposphere of the relationship between (a) the westerly inflow jet (yellow), northerly surface outflow jet (green arrow), lower-tropospheric PV dipole (blue/negative and red/positive), downdraft (brown arrow), and updraft (black arrow); and (b) perspective view showing the airmass pathways, with horizontal reference planes near the surface and 4-km altitude.

of damaging downburst clusters associated with a forward-propagating MCS that, during part of its existence, displays evidence of one or more sustained bow echoes with mesoscale vortices and/or rear-inflow jets. The damage swath must be nearly continuous, at least 100 km wide along most of its extent, and 650 km long."

On 10 August 2020, a derecho formed in northeastern Nebraska at ~1300 UTC [0800 central daylight time (CDT) = UTC − 5 h] and traveled eastward across Iowa, Illinois, Indiana, and western Ohio. Wind damage over 90 000 square miles resulted in $11.5 billion loss in property. Peak wind gusts topped 140 mph in Cedar Rapids, Iowa, and at least 26 tornadoes were spawned. More than 1 000 000 customers lost power, numerous injuries were counted, and four people lost their lives (Chicago Weather Forecast Office 2020).

The Iowa derecho of 10 August 2020 was a high-end event (three or more gusts exceeding 32 m s^{-1}), which occurs every 2–3 years, in a climatological maximum extending from Minnesota southeastward into Indiana, Ohio, and West Virginia (Johns and Hirt 1987; Coniglio and Stensrud 2004; Guastini and Bosart 2016). Summertime configurations favorable to the formation of derechos include an upper-level trough approaching a midtropospheric ridge from the west (Coniglio et al. 2004). As will be shown, the synoptic setting for the 10 August 2020 derecho includes an approaching upper-level cyclone and a lower-tropospheric anticyclone.

To investigate the hypothesis that a downdraft in a derecho is associated with a lower-tropospheric PV dipole, we carried out simulations of the Iowa derecho of 10 August 2020 with the University of Wisconsin Nonhydrostatic Modeling System (UWNMS), which has Ertel's PV as a standard output variable. An idealized diagram of the meridional jet/PV dipole found in UWNMS simulations (Fig. 1) illustrates the basic structure. The westerly inflow jet turns clockwise as it sinks in the downdraft, becoming a northerly jet. The updraft and positive PV anomaly coincide, while the downdraft and negative PV anomaly coincide, with the northerly outflow jet between.

We then investigated the dynamical structure depicted in High-Resolution Rapid Refresh (HRRR) model forecast analyses, which includes absolute vorticity as an output variable. The radar reflectivity pattern of a derecho often evolves from a bow echo to a comma echo (Przybylinski 1995; Weisman and Trapp 2003; Wakimoto et al. 2006; Atkins and St. Laurent 2009). This paper documents the relationship between the updraft/downdraft pair, lower-tropospheric PV dipole, and northerly jet in the 10 August 2020 derecho and its relationship with the characteristic equatorward bulge in the trailing comma radar echo pattern.

The development of a rear-inflow jet is crucial to the formation of a derecho (Weisman 1992, 1993) and the westward tilt with height of the downdraft/updraft pair (Rotunno et al. 1988; Weisman and Rotunno 2004). The gust front updraft is forced by the cold outflow from the downdraft, where lifting of warm, moist air with high potential temperature by the density current leads to instability in the updraft. In an MCS, the degree of westward tilt of the updraft and the shape of the anvil outflow in the UTLS depend on the environmental wind shear profile. Shallow shear tends to promote a strongly sloping front-to-rear flow with an extensive anvil developing to the west and trailing stratiform precipitation, while deep shear tends to promote an extensive anvil developing to the east and leading stratiform precipitation (Lin 2007).

The existence of a critical level at which the ambient wind speed U is equal to the phase speed of the derecho c implies that there is a steering level for the storm (Lin 2007). This also implies that latent heating in the updraft and downdraft can effectively amplify the interaction between the updraft and the downdraft. In an idealized modeling study, Weisman and Rotunno (2004) found that, when shear in the lowest 5 km is increased from 10 to 20 m s^{-1} (5 km)$^{-1}$, the updraft becomes more upright, with a stronger forward anvil outflow. At this level of shear, there is still significant front-to-rear outflow. However, with a low-level shear of 30 m s^{-1} (5 km)$^{-1}$ the front-to-rear flow disappears and the updraft is nearly upright. This suggests that a low-level shear of ~20–25 m s^{-1} (5 km)$^{-1}$ might be optimal for a derecho, fostering longevity through structural stabilization, with positive feedback between forced condensation and hydrometeor cooling. The inflow jet experiences diabatic cooling and drag by hydrometeors in the downdraft (Markowski and Richardson 2010; Seigel and van den Heever 2013), which transports midtropospheric air with high momentum to near the surface and creates a cold pool.

Since nearly straight-line motion is an essential aspect of a derecho, most studies have focused on motions in longitude–altitude. However, Evans et al. (2014) describe a family of trajectories in a derecho which "descend from the north and northwest." In this study, we explore the role of the meridional wind component and its relationship with PV structures, updrafts, downdrafts, and shape of the trailing comma echo.

Lin and Smith (1986) investigated the response to a traveling region of cooling associated with falling hydrometeors in the downdraft of a squall line, which included a westward-tilted updraft/downdraft pair and source of gravity wave activity. The simultaneous formation of gravity waves and updraft/downdraft pair has been studied by Bretherton and Smolarkiewicz (1989), Pandya et al. (2000), Shige and Satomura (2000), Fovell et al. (2006), Lane and Zhang (2011), and Adams-Selin (2020).

Raymond and Jiang (1990) proposed that an MCS can maintain itself over a long period of time through interaction between the diabatic effects of moist convection and the vertical motion field. They explored the contribution of diabatic heating in producing mesoscale PV anomalies by transporting mass across isentropic surfaces [see also Haynes and McIntyre (1990)]. Fritsch et al. (1994), Jiang and Raymond (1995), Wernli and Davies (1997), Lin (2007), and Chagnon and Gray (2009) found that diabatic vortex stretching in an updraft will generate a positive PV anomaly below the heating maximum. In a negative buoyancy-driven downdraft, diabatic vortex shrinking will occur below the level of maximum cooling (Lin and Smith 1986), producing a negative PV anomaly in the lower troposphere. In examining PV tendency in convective situations, other authors have shown that the diabatic tilting term is important when there is significant vertical shear (Chagnon and Gray 2009; Weijenborg et al. 2017; Oertel et al. 2020; Harvey et al. 2020; Prince and Evans 2022).

It is helpful for discussion to introduce the conservation equations for PV and absolute vorticity, since UWNMS output fields include Ertel's PV at constant altitude, while HRRR output fields include absolute vorticity at constant pressure. The vertical component of Ertel's PV is $P = [(1/\rho_o)(\partial\theta/\partial z)(f+\zeta)] - [(1/\rho_o)(\partial\theta/\partial x)(\partial v/\partial z)] + [(1/\rho_o)(\partial\theta/\partial y)(\partial u/\partial z)]$, where relative vorticity is $\zeta = (\partial v/\partial x) - (1/\cos\phi)[\partial(\cos\phi u)/\partial y]$, θ is potential temperature, f is the Coriolis parameter, ρ_o is the basic-state density, $\partial x = a\cos\phi\partial\lambda$, and $\partial y = a\partial\phi$ [Eq. (3.1.4) in Andrews et al. 1987]. Neglecting the net viscous force, the effects of diabatic stretching and diabatic tilting on PV following the motion are given by

$$\frac{DP}{Dt} = \frac{1}{\rho_o}\left[(f+\zeta)\frac{\partial Q}{\partial z} + \frac{\partial Q}{\partial y}\frac{\partial u}{\partial z} - \frac{\partial Q}{\partial x}\frac{\partial v}{\partial z}\right], \tag{1}$$

where Q is the diabatic heating [derived from Eq. (3.1.5) in Andrews et al. 1987]. Although Q is not available as an output field for the UWNMS, we can use scale analysis to estimate the likely relevance of the diabatic stretching and tilting terms. Neglecting friction and solenoidal terms, the tendency equation for absolute vorticity following the motion is

$$\frac{d}{dt}(\zeta+f) = (\zeta+f)\frac{\partial w}{\partial z} + \frac{\partial w}{\partial y}\frac{\partial u}{\partial z} - \frac{\partial w}{\partial x}\frac{\partial v}{\partial z} \tag{2}$$

(Holton and Hakim 2013). Since $w(\partial\theta/\partial z) \approx Q$ in convection, similar scaling arguments can be made for PV and absolute vorticity.

Considering the diabatic stretching term $(1/\rho_o)(f+\zeta)(\partial Q/\partial z)$, below a heating maximum in an updraft, $\partial Q/\partial z > 0$ will induce a region of $P > 0$. Below a cooling maximum in a downdraft, $\partial Q/\partial z < 0$ will induce a region of $P < 0$ (Lin and Smith 1986). Typical magnitudes may be estimated near 700 hPa, where $\rho \sim 0.8$ kg m^{-3}. If we assume that $f + \zeta \sim 10^{-4}$ s^{-1}, $Q \sim \pm 10$ K h^{-1}, and $\delta z \sim 3$ km, the resulting PV tendency would be $\sim \pm 0.4$ PVU h^{-1}.

To estimate the diabatic tilting term $-(1/\rho_o)(\partial Q/\partial x)(\partial v/\partial z)$ near 700 hPa, if $Q \sim 10$ K h^{-1}, $\delta x \sim 50$ km, and $\partial v/\partial z \sim 20$ m s^{-1} (5 km)$^{-1}$, and if the two gradient fields are in phase, the diabatic tilting tendency would be $\sim \pm 1$ PVU per hour. Near the tropopause (150 hPa), $\rho \sim 0.2$ kg m^{-3}. If $Q \sim 1$ K h^{-1}, $\delta x \sim 50$ km, and $\partial v/\partial z \sim 30$ m s^{-1} (2 km)$^{-1}$ in the UTLS, the diabatic tilting tendency would be $\sim \pm 1.5$ PVU h^{-1}. Once PV anomalies are formed by diabatic stretching and diabatic tilting, they can be advected upward or downward along isentropes.

Evans et al. (2014) carried out a PV analysis for the formation of the cyclonic mesobeta vortex at the north end of the bow echo in the Super Derecho of 8 May 2009 (Weisman et al. 2013). Xu et al. (2015) studied the genesis of mesovortices in the bow echo system of this derecho using a model with a 4-km outer grid and 0.8-km inner grid. They found a long-lived cyclonic mesovortex near the cusp of the bow echo which is somewhat similar to the east (cyclonic) half of the PV dipole to be described below. In the present study, an east–west-oriented PV dipole is diagnosed, with a northerly jet between. To our knowledge, this structure has not been previously described in the literature.

The observations, UWNMS simulations, and HRRR analyses provide complementary information. The UWNMS, with explicit moist convection, includes Ertel's PV, equivalent potential temperature θ_e, and streamfunction as output variables and evolves without updating information in the interior. HRRR ingests radar and satellite data in a rapid update cycle and includes absolute vorticity as an output variable. This provides the opportunity for comparison of the location, rate of progression of the derecho, and dynamical structure.

Can a derecho can be produced in a model internally from "first principles" and a suitable initial state, or does one need to ingest detailed observations during integration to achieve a reasonable derecho structure? Requisite elements include a sufficiently moist environment, forcing which provides uplifting, and environmental shear which helps to organize the storm. We investigated this by running the UWNMS using relatively coarse initialization data and updating only on side boundaries. The mesoscale detail that evolves in the UWNMS is a dynamically distinct solution relative to HRRR, which incorporates high-resolution 3D information into the interior of the grid throughout integration. If similar PV structures are found in the HRRR and UWNMS, this would support the robustness of the result.

The observational datasets, HRRR analyses, and UWNMS simulations used in this study are described in section 2. A depiction of the derecho as seen in ground-based and satellite observations is given in section 3, including the temporal signature of the northerly jet at Des Moines and the shape of the outflow cirrus. HRRR synoptic-scale wind analyses at tropospheric pressure levels show the relationship between the approaching upper-level cyclone, westerly inflow jet, and surface anticyclone. The evolution of three simulations is described in section 4. The PV dipole/meridional jet structure, relationship with updraft/downdraft pair, and westerly inflow jet are shown for UWNMS simulations in section 5 and for HRRR in section 6. Dynamical aspects discussed in section 7 include the role of the inflow jet in determining the speed and strength of the derecho, critical level theory, and the generation mechanism for the lower-tropospheric PV dipole. Results are summarized in section 8.

2. Observations, HRRR analysis, and UWNMS simulations

a. *Radiosonde, surface, radar, and satellite observations*

Hourly radar plots were used to estimate the rate of eastward progression of the gust front. A surface station map was generated for 1600 UTC (1100 CDT) 10 August 2020, when the gust front reached Des Moines, Iowa. A special sounding was taken at Davenport, Iowa (DVN), at 1700 UTC (1200 CDT), about 2 h before the arrival of the gust front.

Surface observations at 1-min interval were obtained for Des Moines, Iowa (DSM), for the 12-h period 1200–2400 UTC (0700–1900 CDT) 10 August 2020. Both 1-min average wind speed ("wind speed") and "gust speed" were obtained, along with 1-min average wind direction. The National Weather Service defines a 2-min average gust speed as "the values of the 3-s peak from the 5-s sample containing the highest 3-s peak wind speed." The Iowa Mesonet provided a 1-min average gust speed.

Lightning strikes detected by the *GOES-16* Geostationary Lightning Mapper (GLM) during a 20-s period were superimposed on *GOES-16* Advanced Baseline Imager (ABI) L2 images of cloud-top temperature and height at ~1800 UTC (~1300 CDT).

b. *HRRR forecast analyses*

HRRR model forecast analyses were obtained from NOAA. The HRRR model has 3-km grid spacing, with radar data assimilated every 15 min over a 1-h period (Dowell et al. 2022). The HRRRv4 CONUS domain, with 1800 × 1060 grid points, spans the contiguous United States. We analyzed the HRRR forecast starting at 0000 UTC 10 August 2020. Three-dimensional isosurfaces were created using MATLAB.

c. *The UWNMS*

The UWNMS (Tripoli 1992a,b) was derived from the CSU model of Tripoli and Cotton (1982) and was designed to study the interaction between convection and its environment. We have used it to study inertial instability and midlatitude jets (Rowe and Hitchman 2015, 2016), UTLS PV dipoles (Hitchman and Rowe 2017, 2019), summertime flooding (Rowe and Hitchman 2020), and tropopause folds (Hitchman and Rowe 2021).

TABLE 1. Specifications for UWNMS simulations.

Model	UWNMS version 8i
Time	0000 UTC 10 Aug 2020 initialization, run 24 h, output every 20 min
Grid	Domain 1200 km × 1200 km, spherical grid center point 41°N, 91°W 300-m vertical grid spacing, 95 vertical levels, five soil grid points 26.7-km model top with 1.5-km Rayleigh friction sponge layer 85 vertical grid points in visualized domain (25.2-km top)
Physics	Explicit convection, turbulent kinetic energy prediction Hashino and Tripoli's (2007, 2011) microphysics Lateral and upper boundaries—Hack/Schubert normal mode method
Initialization	0.5°NCEP GFS data, boundary values updated every 15 min
Runs	UWNMS-4 UWNMS-8

For the derecho simulations, the UWNMS was initialized with 0.5° data from the National Centers for Environmental Prediction (NCEP) Global Forecast System (GFS) at 0000 UTC 10 August and run for 24 h, updating boundary conditions every 15 min (Table 1).

We used a domain of 1200 km × 1200 km centered in eastern Iowa (41°N, 91°W), covering 36°–46°N and 84°–98°W. Simulations were carried out with 4-, 6-, 8-, 10-, and 12-km grid spacing, keeping all other parameters constant. The coherence of a derecho-like structure generally improved with smaller grid spacing (not shown). Each simulation exhibited a different evolution history, with significant variation in amplitude and structure with time within each simulation. In section 5, results are shown for simulations with grid spacings of 4 km (UWNMS-4) and 8 km (UWNMS-8).

3. Observational depiction of the Iowa Derecho of 10 August 2020

a. *Evolution of the gust front*

An hourly sequence of radar reflectivity images during 1250–2350 UTC 10 August 2020 (Fig. 2) shows that the derecho reached Des Moines at 1600 UTC (Fig. 2e) and Davenport, Iowa, at 1900 UTC (Fig. 2h). Gusts in the range of 25–40 m s^{-1} were observed across Iowa during 1500–1900 UTC (Iowa Environmental Mesonet). This derecho developed a comma echo, with an initially linear convective cluster extending to the northeast (Fig. 2). An equatorward bulge of the echo pattern developed as the derecho propagated into Illinois and Indiana (Figs. 2h–m). The leading edge of the comma traveled toward the east, but the surface outflow behind the gust front was northerly.

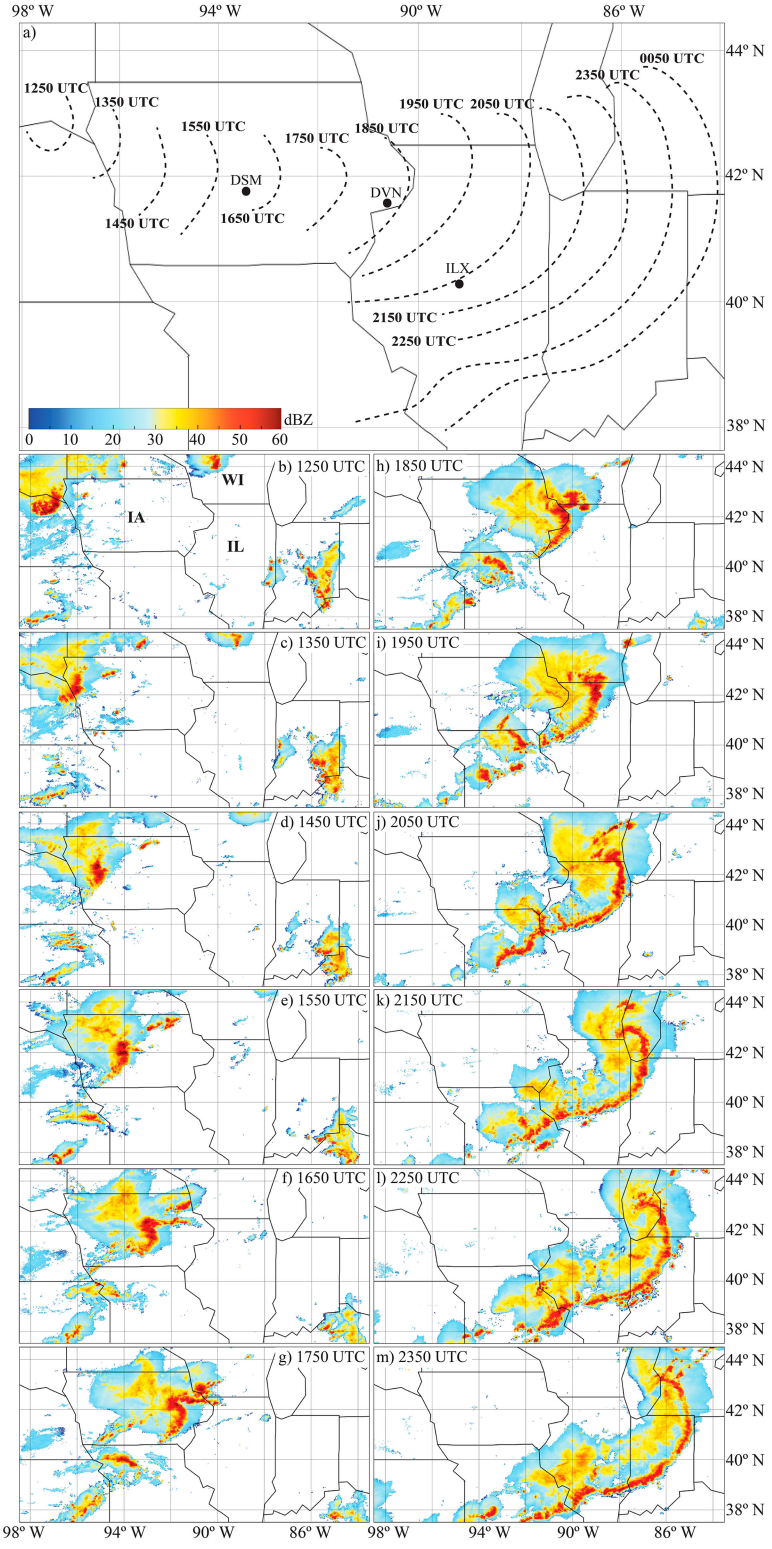

FIG. 2. (a) Progression of the arc of high reflectivity from 1250 UTC 10 Aug to 0050 UTC 11 Aug 2020 (0750–2050 CDT 10 Aug). (b)–(m) Hourly snapshots from 1250 to 2350 UTC. The locations of Des Moines, Iowa (DSM); Davenport, Iowa (DVN); and Lincoln, Illinois (ILX) are indicated in (a). Values of dBZ less than zero are not plotted.

Campbell et al. (2017) used "the approximate center of the leading edge of the feature of interest" to define derecho speed. Here, we track the easternmost point of the echo pattern (Fig. 2a). The eastward speed was ~18 m s^{-1} at 1400 UTC, increasing to ~30 m s^{-1} at 1900 UTC, and then decreasing to ~21 m s^{-1} by 2300 UTC, with a mean of 24.5 m s^{-1} (Fig. 3a).

Mahoney et al. (2009) compared the speed of propagation of MCSs with maximum zonal wind speed in the cold pool and mean 900–200-hPa wind speed. They found speeds of 10–22 m s^{-1}, similar to the maximum zonal wind speed in the cold pool. Corfidi et al. (1996) defined the advective component of an MCS to be proportional to the mean wind in the 850–300-hPa layer. In section 4, we will compare the speed of the gust front with the speed of the 850–700-hPa westerly inflow jet. The 850–700-hPa (~3–5 km) layer was chosen because it is the layer of maximum westerly flow in this case. It can be related to critical surface theory for low-level shear, where the outflow pattern in the upper troposphere depends on how low-level shear influences storm structure.

b. *Surface station chart*

At 1600 UTC 10 August 2020, a cold front extended from Kansas to Wisconsin (Fig. 3b). Dewpoint temperatures T_d exceeded 75°F (24°C) over Iowa and most of Illinois, with values near 64°F (18°C) along the cold front and less than 60°F (16°C) to the north and west of Iowa (Fig. 3b).

c. *Davenport, Iowa, sounding at 1700 UTC*

In the 1700 UTC DVN sounding (Fig. 3c), the level of free convection (LFC) was ~2200 m and the equilibrium level (EL) was ~14 760 m, for a moderate CAPE value of ~1700 J kg^{-1}. However, Evans and Doswell (2001) found that when synoptic-scale forcing is strong, derechos can develop and persist within environments with almost no CAPE evident on nearby soundings. From the surface to 3 km, the wind speed increased upward by ~15 m s^{-1} (wind shear ~ 5×10^{-3} s^{-1}), shifting from southwesterly to westerly. Dry air with southwesterly flow is seen in the 6.5–8-km layer, above which the flow becomes increasingly westerly, reaching ~35 m s^{-1} near the tropopause (~12 km). In the 300–100-hPa layer, there are alternating layers of stronger and weaker westerlies (Fig. 3c).

d. *Satellite cloud-top images*

At 1800 UTC, the outflow gust front was located near 91.5°W, about an hour west of Davenport, Iowa (Fig. 2g). A region of cloud-top temperatures less than 210 K (Fig. 4a) and cloud-top heights exceeding 16 km (Fig. 4b) is seen over east-central Iowa, with coincident lightning (Figs. 4a,b), indicating the presence of deep convection. The cirrus outflow boundary coincides approximately with the 240-K contour. The cirrus shield extends westward over Iowa, with the trailing stratiform region overlying the midlevel inflow jet (Smull and Houze 1987; Adams-Selin and Johnson 2013), as well as northward over Minnesota and northeastward over Wisconsin. The shape of the cirrus shield is consistent with a vertical wind profile which allows for significant outflow both upstream and downstream in the UTLS.

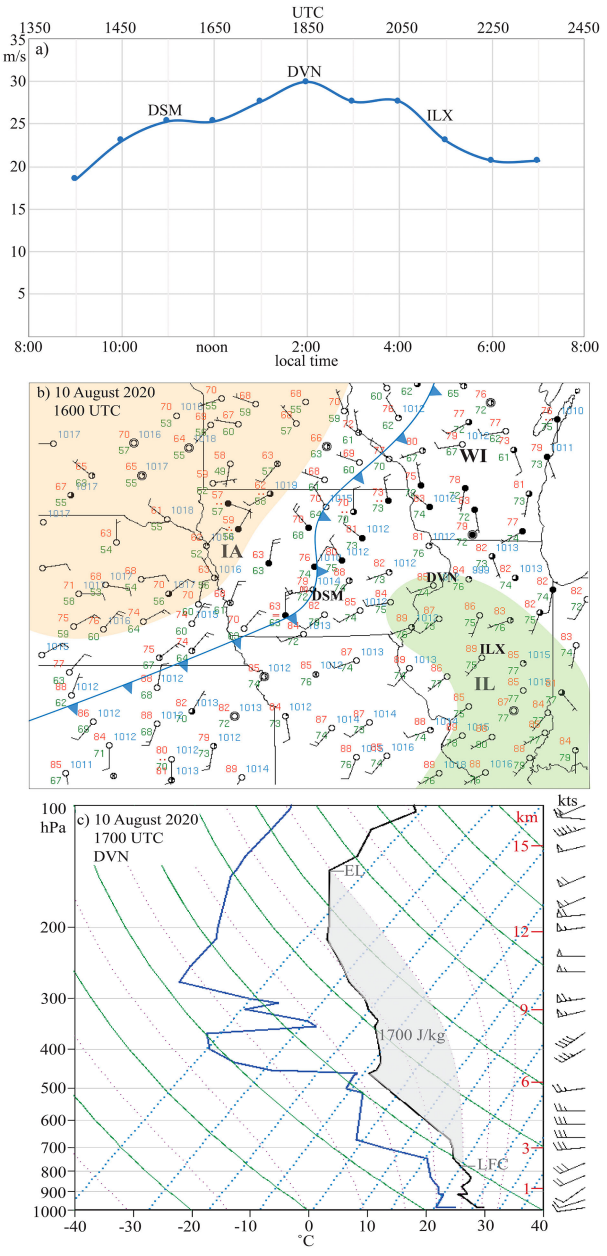

FIG. 3. (a) Speed of propagation during 1400 UTC 10 Aug–0000 UTC 11 Aug 2020 (0900–1900 CDT 10 Aug). Approximate arrival times at DSM, DVN, and ILX are indicated. (b) Surface station plot for 1600 UTC (1100 CDT) 10 Aug 2020. The position of the cold front is shown. Dewpoint temperatures exceeding 75°F are shaded light green, less than 65°F light brown. The locations of Iowa (IA), Wisconsin (WI), and Illinois (IL) are indicated, along with stations DSM, DVN, and ILX. (c) National Weather Service special sounding from Davenport, Iowa (DVN), at 1700 UTC (1200 CDT) 10 Aug 10 (about 2 h before the arrival of the derecho). Profiles of temperature (°C; dark blue), dewpoint temperature (°C; light blue), and horizontal wind vectors (kt) are shown. The LFC, EL, and CAPE are indicated.

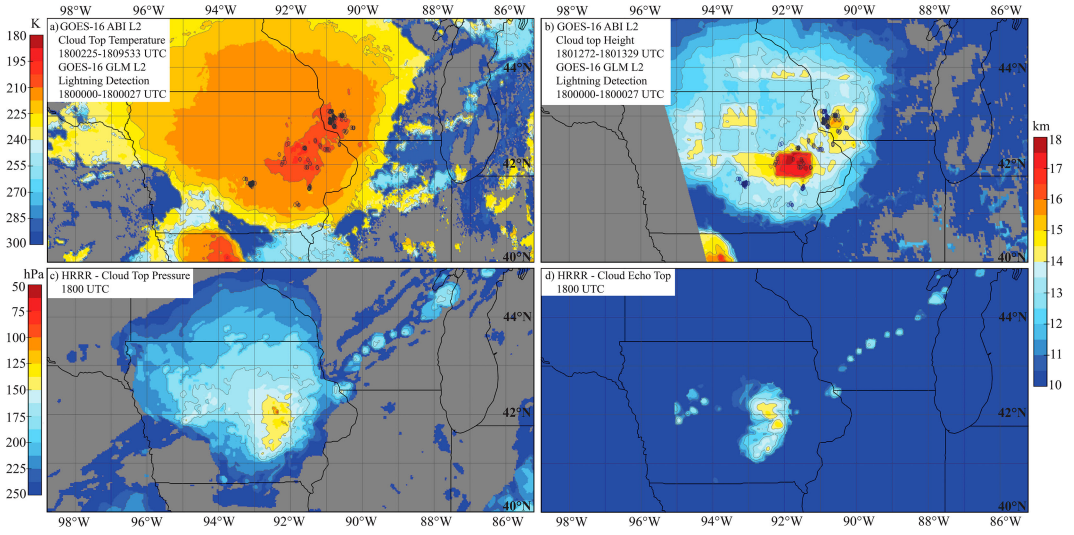

FIG. 4. (a) *GOES-16* ABI-L2 cloud-top temperature (K), (b) *GOES-16* ABI-L2 cloud-top altitude (km), (c) HRRR cloud-top pressure (hPa), and (d) HRRR cloud-top echo altitude (km) at 1800 UTC 10 Aug 2020. The locations of lightning strikes detected by the *GOES-16* GLM during the 20-s period 1759:40–1800:00 UTC are shown with black dots.

In HRRR, similar features are indicated, but the region of lowest cloud-top pressure (Fig. 4c) and highest cloud-top echo height (Fig. 4d) is located ~80 km to the west and ~25 km to the south. In addition, the line of convective activity extending eastward over northern Illinois in satellite observations (Figs. 4a,c) and radar reflectivity (Fig. 2g) instead extends northeastward across Wisconsin in the HRRR analyses (Figs. 4b,d).

The coldest cloud-top satellite temperatures are less than 200 K, and the highest altitudes occur at 18.0 km (~55 000 ft) (Figs. 4a,b). In HRRR, the lowest cloud-top pressure is 90 hPa and the highest cloud-top echo height is 15.3 km (Figs. 4c,d).

e. Surface observation time series at Des Moines

During 1200–1530 UTC, maximum gusts at Des Moines were ~5 m s^{-1} or less (Figs. 5a,b), with the surface wind direction shifting gradually from southerly to westerly (Fig. 5b). During 1400–1530, UTC surface pressure rose gradually, with a series of oscillations with amplitude ~0.5 hPa and period of ~15–30 min (Fig. 5a).

Around 1600 UTC, gust speed at DSM increased from westerly at ~5 m s^{-1} to northerly at ~33 m s^{-1} in less than 10 min (Fig. 5b). Typical gust speeds are ~30%–50% higher than 1-min average wind speeds (not shown). After 1600 UTC, the wind speed decreased exponentially to ~12 m s^{-1} in an hour (Fig. 5a). Northerly flow exceeded 22 m s^{-1} for ~20 min. With an eastward translation speed of 28 m s^{-1} for the derecho past Des Moines, this duration implies a ~35-km zonal width for the meridional jet exceeding 22 m s^{-1}. The duration of northerly flow exceeding 15 m s^{-1} implies a zonal width of ~90 km. During 1600–1800 UTC, the wind direction shifted gradually from north-northwesterly (~345°) to northeasterly (~60°), held steady during 1800–1930 UTC, and then abruptly switched to southerly upon arrival of the west end of the cold pool (Figs. 5b,c). Over the subsequent 5 h, winds gradually shifted to northwesterly (Fig. 5b).

An increase in surface pressure of ~5 hPa occurred over ~15 min (~0.5 Pa s^{-1}) near 1600 UTC (Fig. 5a). The peak in pressure occurred ~5 min after the peak in wind speed. This is consistent with an outflow boundary "pressure head," with a sharp eastward decrease in pressure accelerating the flow ahead of the pressure maximum (e.g., Fig. 6.8 of Lin 2007). The period of elevated pressure lasted ~2.5 h (Fig. 5a). The 3.5-h period 1600–1930 UTC is characterized by northerly surface flow (Fig. 5b).

During 1200–1530 UTC, the temperature rose from 73° to 81°F (23°–27°C), while T_d held steady near 71°F (22°C) (Fig. 5c). With the arrival of the gust front at 1600 UTC, temperatures dropped to ~62°F (17°C) in ~20 min and T_d dropped to ~60°F (16°C). In the wake of the initial outflow boundary and downburst, temperatures gradually returned to 79°F (26°C) over the next 7 h (Fig. 5c). The dewpoint stayed low during the ~3.5-h duration of the cold pool and then rose slightly, but remained below 65°F (18°C).

This sharp northerly jet (Fig. 5b) implies the existence of a relative vorticity dipole in the lower troposphere, with a positive leading anomaly to the east and a negative anomaly to the west (Fig. 1).

f. HRRR wind charts

At 1800 UTC 10 August 2020, a synoptic-scale trough is seen at 150 hPa over the upper Midwest, with southwesterly flow over eastern Iowa and Wisconsin (Fig. 6a). This flow is interrupted by a mesoscale region of low-speed air at 42°N, 92.5°W (Fig. 6a). At 300 hPa, stronger winds are evident in the trough and the mesoscale region of low-speed air is larger, with noticeable outflow toward the north (Fig. 6b).

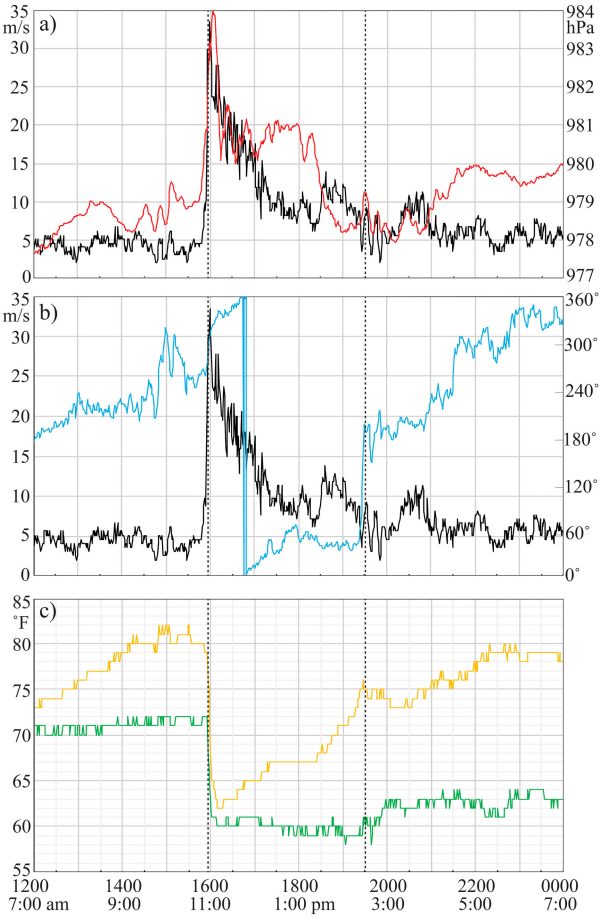

FIG. 5. Iowa Environmental Mesonet surface meteorological observations at Des Moines, Iowa (DSM), during 1200–2400 UTC (0700–1900 CDT) 10 Aug 2020 of (a) surface pressure (red line) and gust speed (black), (b) gust speed (black) and wind direction (blue), and (c) temperature (yellow) and dewpoint temperature (green). Data are shown at 1-min intervals. Vertical dashed lines indicate the duration of the cold pool at DSM.

The wind pattern at 500 hPa shows an approaching jet streak, extending from the northwest into western Iowa, in a meridionally concentrated band about ~200 km wide (Fig. 6c). A minimum in wind speed is again seen near 42°N, 92.5°W (Fig. 6c). At 700 hPa, flow converges into the westerly inflow jet, exceeding 25 m s^{-1} over central Iowa (Fig. 6d). An anticyclonic flow pattern is found to the west at 850 hPa (Fig. 6e), with northerly flow entering northwestern Iowa. Note also the mesoscale region of westerlies at 850 hPa exceeding 35 m s^{-1} over eastern Iowa (Fig. 6e). At 950 hPa, continuous northerly flow extends from Minnesota to southern Iowa (Fig. 6f), with a comma-shaped speed maximum consistent with the abrupt switch to northerly flow seen at Des Moines (Figs. 5b and 6f). From 700 to 950 hPa, the speed maximum turns from westerly to northerly (Figs. 6d–f). The mesoscale northerly jet at 950 hPa is continuous with the northerly outflow from the anticyclone to the north (Fig. 6f).

4. Comparison of storm evolution

The evolution of hourly samples in updraft speed during the life of the derecho for UWNMS-4 and UWNMS-8 at 3-km altitude, and for HRRR at 700 hPa, is shown in Fig. 7a. In HRRR analyses, starting at 1400 UTC, updraft speed increased from ~0.3 to ~3.5 m s^{-1} by 1700 UTC and then gradually declined to ~1 m s^{-1} at 2000 UTC, with a second peak of ~3.5 m s^{-1} at 2100 UTC (Fig. 7a). In the UWNMS-4 simulation, updraft speed was negligible at first, increasing from ~0 to ~3 m s^{-1} during 1500–1700 UTC. It then generated an unrealistically strong updraft (>14 m s^{-1}) at 1800 UTC, followed by a pronounced minimum in speed at 1900 UTC and then a resurgence to ~8 m s^{-1} at 2000 UTC (Fig. 7a). In the UWNMS-8 simulation, the development of the updraft was delayed by 2–3 h, finally strengthening to 1 m s^{-1} at 1800 UTC, then ~4 m s^{-1} at 1900 UTC, and remaining strong for four hours (Fig. 7a).

The average eastward speed of the gust front was observed to be 24.5 m s^{-1} during 1400–2300 UTC and 28.0 m s^{-1} during 1700–2100 UTC (Figs. 3a and 7b). Hourly sections of zonal wind along 42°N in HRRR (Fig. S1 in the online supplemental material) were used to make a separate estimate of the speed of propagation, which is ~5 m s^{-1} less than deduced from radar echoes (Fig. 7b). The average speed of the westerly inflow layer in the 750–500-hPa layer 100 km west of the gust front in HRRR grows and then weakens, similar to gust front speed, but it is ~5–10 m s^{-1} slower (Fig. 7b). The westerly wind in UWNMS-8 at 4.5-km altitude sampled 50 km upstream and 50 km poleward of the gust front shows better agreement with the observed speed of the gust front (Fig. 7b). These results may be compared with Fig. 7 of Mahoney et al. (2009).

The evolution history in each of the three simulations was quite distinct. The UWNMS-4 simulation initially showed similar development to HRRR but then underwent two large amplification/diminution cycles. The UWNMS-8 simulation developed too slowly but then achieved an updraft strength comparable to HRRR, with a coherent structure lasting for ~5 h.

5. Depiction of structure in UWNMS simulations

The center of the updraft/downdraft pair in both UWNMS simulations propagated nearly eastward along 42°N, with the timing of primary dynamical features similar to the gust front seen in radar reflectivity (Fig. 2) and Des Moines surface data (Fig. 5). The two simulations differ in the timing of amplification and in the degree of westward tilt with height.

During 1800–2000 UTC, both UWNMS simulations show an east–west PV dipole, with the leading positive PV member of the dipole coinciding with the updraft and the trailing negative PV member coinciding with the downdraft (Fig. 8). During 1800–2000 UTC, there is a transition in the UWNMS-4 from a strong updraft burst subsiding into a dispersed set of mesoscale convective vortices (MCVs; Figs. 7a and 8a–c), but in the UWNMS-8 a derecho-like structure grows to moderate, steady strength (Figs. 7a and 8d–f).

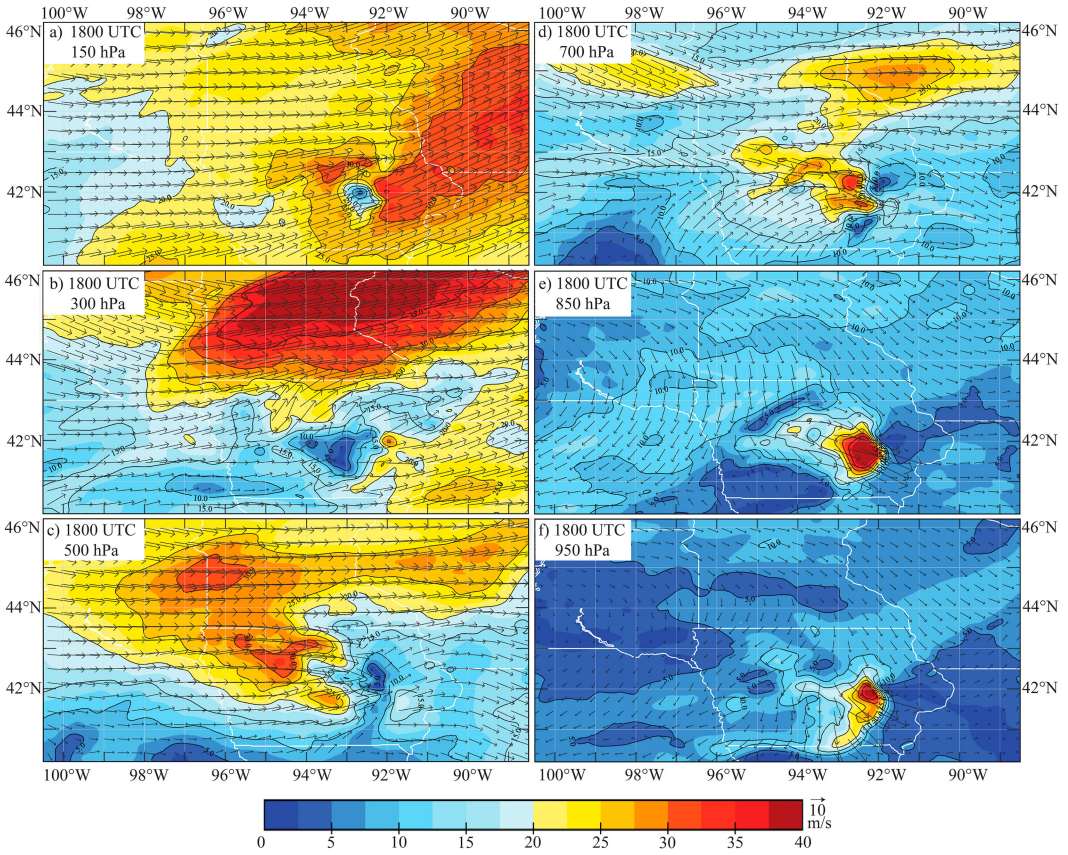

FIG. 6. HRRR horizontal wind speed (color bar; interval 2.5 m s^{-1}) and wind vectors (reference length 10 m s^{-1}) at 1800 UTC 10 Aug 2020 for (a) 150, (b) 300, (c) 500, (d) 700, (e) 850, and (f) 950 hPa.

The robustness of the lower-tropospheric PV dipole structure is dependent on a sufficiently strong and vertically continuous updraft/downdraft pair. For example, at 1800 UTC a PV dipole in UWNMS-4 is apparent (Fig. 8a), with an updraft speed exceeding 14 m s^{-1} (Fig. 7a), but at 1900 and 2000 UTC there is instead a set of smaller-scale MCVs arranged along the outflow boundary (Figs. 8b,c), with updraft speeds of less than 2 m s^{-1} at 1900 UTC (Fig. 7a).

In contrast, UWNMS-8 showed a steady derecho-like structure during 1900–2100 UTC (Figs. 8d–f), with an updraft speed of ~5 m s^{-1} (Fig. 7a) and a lower-tropospheric PV dipole coincident with the downdraft/updraft pair. In UWNMS-8, during 1800–2000 UTC the negative PV anomaly grew from ~−1 to −2 PVU, while the downdraft grew from ~−1 to −2 m s^{-1}, and the positive PV anomaly grew from ~0.5 to 2 PVU, while the updraft grew from ~0.6 to 4 m s^{-1} (Figs. 8d–f). It will be shown that these values of vertical motion and PV anomalies are similar to those in HRRR, with similar horizontal scales of ~50 km.

To illustrate the range in structure of PV and 3D winds in the UWNMS, and for comparison with HRRR structure and with shear theory, we chose a high-amplitude state of the UWNMS-4 at 1800 UTC (Fig. 9) and a representative state of the UWNMS-8 at 1900 UTC (Figs. 10–12).

Longitude–altitude sections of UWNMS-4 variables along 42°N (Fig. 9) are shown with an aspect ratio of 2:1 in the domain 0–21-km altitude, 95.0°–90.5°W, to facilitate comparison with HRRR. The location of this section was chosen to fit the locus of updraft/downdraft and PV dipoles in the UWNMS (inset, Fig. 9b). The meridional deviation from 42°N of the track of the center of the PV dipole was less than 5 km as it progressed across the domain.

The location of the gust front can be determined from where the northerly flow maximum abruptly increases, near 91.5°W at 1800 UTC (Fig. 9b). A westerly inflow jet exceeding 25 m s^{-1} is seen in the 4–6-km layer about 50 km to the west of the gust front. This pattern extends down to near the surface, with zonal winds exceeding 30 m s^{-1} (Fig. 9a) and meridional winds exceeding −25 m s^{-1} (Fig. 9b). This descent of the westerly inflow layer in UWNMS-4 occurs fairly abruptly, and the updraft is nearly upright (Fig. 9c). The surface westerly and northerly jet maxima coincide with the downdraft (Figs. 9a–c). The northerly jet extends upward to 10-km altitude. It lies between a PV dipole of −10/+20 PVU maximizing near 7 km (Figs. 8b,d).

The updraft in UWNMS-4 exceeds 25 m s^{-1} and reaches 14-km altitude (Fig. 9c). The westerly inflow jet, with $\theta_e < 330$ K (Figs. 9a,c), splits near 8-km altitude, with a weak rising branch joining the main updraft (Fig. 9c). In the UTLS, a westward outflow layer is found near 12-km altitude and a strong eastward outflow layer exceeding 70 m s^{-1} is found near 14 km

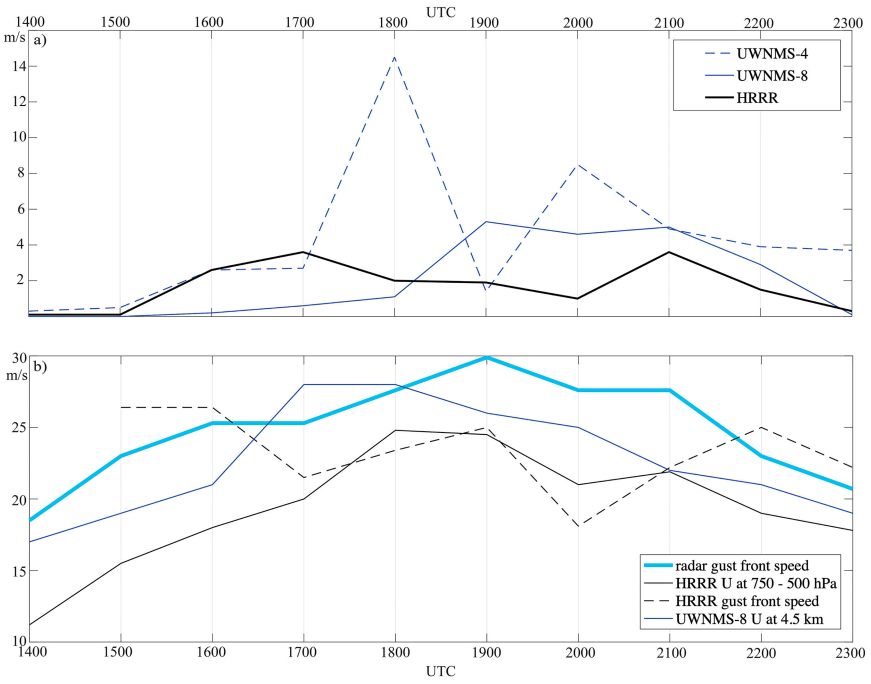

FIG. 7. Hourly time series during the period 1400–2300 UTC 10 Aug 2020 of (a) maximum updraft velocity (m s^{-1}) along 42°N at 700 hPa for HRRR (thick black) and at 3.18-km altitude for UWNMS-4 (dashed blue) and UWNMS-8 (blue) simulations and (b) radar gust front speed from Fig. 3a (m s^{-1}; thick blue), HRRR zonal wind speed 100 km upstream of the gust front averaged in the 500–700-hPa layer (black), gust front speed estimated from HRRR surface wind pattern (dashed black), and UWNMS-8 zonal wind speed at 4.5-km altitude 50 km upstream and 50 km poleward of the gust front (blue).

(Fig. 9a). The zonal flow in the updraft is markedly easterly (Fig. 9a), with flow reaching −20 to −30 m s^{-1} in the upper troposphere, extending to 16 km, and coinciding with southerly flow (Fig. 9b).

An east–west PV dipole is seen in the 14–16-km layer at the top of the updraft (Fig. 9d). The wavy pattern in potential temperature and PV which tilts westward with height into the stratosphere (Figs. 9c,d) represents upward propagation of gravity wave activity and downward transport of westerly momentum.

The updraft/downdraft pair in UWNMS-4 at 1800 UTC exhibits weak westward tilt with height (Fig. 9c), consistent with a weak and variable cold pool below 800 hPa near 92°–94°W (Fig. 9c). The influence of convection can be seen up to ~18 km (Fig. 9), which is a higher altitude than the maximum HRRR cloud-top echo height (Fig. 4d), but is similar to satellite observations (Fig. 4b).

In UWNMS-8, the updraft/downdraft pair at 1900 UTC exhibits a stronger westward tilt with height (Fig. 10). At 1900 UTC, the gust front was located near 90.5°W (Figs. 10a,b). A westerly inflow jet of ~25 m s^{-1} is seen in the 4–6-km layer about 50 km to the west of the gust front, which extends continuously down to near the surface and coincides with a northerly jet exceeding −18 m s^{-1} near 2-km altitude (Fig. 10b). The surface westerly and northerly jet maxima occur in the vicinity of the downdraft (Figs. 10a–c).

In UWNMS-8, the northerly jet lies between a PV dipole of −1/+4 PVU, which maximizes near 6 km (Figs. 10b,d). The axis of maximum northerly wind (Fig. 10b) lies between the updraft/downdraft pairs (Fig. 10c) and between the PV dipoles (Fig. 10d), separating the westerly inflow layer from the westward-tilting updraft (Fig. 10a).

In UWNMS-8 at 1900 UTC, the northerly jet extends upward to ~7 km and the updraft extends to ~12-km altitude (Fig. 10c), exhibiting less vertical development compared with UWNMS-4 at 1800 UTC (Fig. 9c). The updraft (Fig. 10c), axis of maximum northerly flow (Fig. 10b), separation between strong and weak westerlies (Fig. 10a), and the PV dipole all tilt westward with height by ~–30 km in 10-km altitude, with an elevation angle of ~17° (Fig. 10a). It will be shown that this is comparable to the tilt of the updraft in HRRR (~15°), but the elevation angle of the downdraft is much smaller in HRRR (~1.7°).

The horizontal extent of the updraft and downdraft in UWNMS-8 near 3 km at 1900 UTC (Fig. 10c) is ~30 km, similar to scales depicted in Smull and Houze (1987). In UWNMS-8, a cold pool with $\theta_e < 340$ K is seen to the west of the gust front (91.2°–90.8°W) below 800 hPa, which is somewhat more realistic than in UWNMS-4 (Fig. 9c). Note also values of $\theta_e > 350$ K in the boundary layer ahead of the gust front (Fig. 10c).

In UWNMS-8 at 1900 UTC, an easterly front-to-rear outflow layer occurs near 9-km altitude, with a westerly outflow

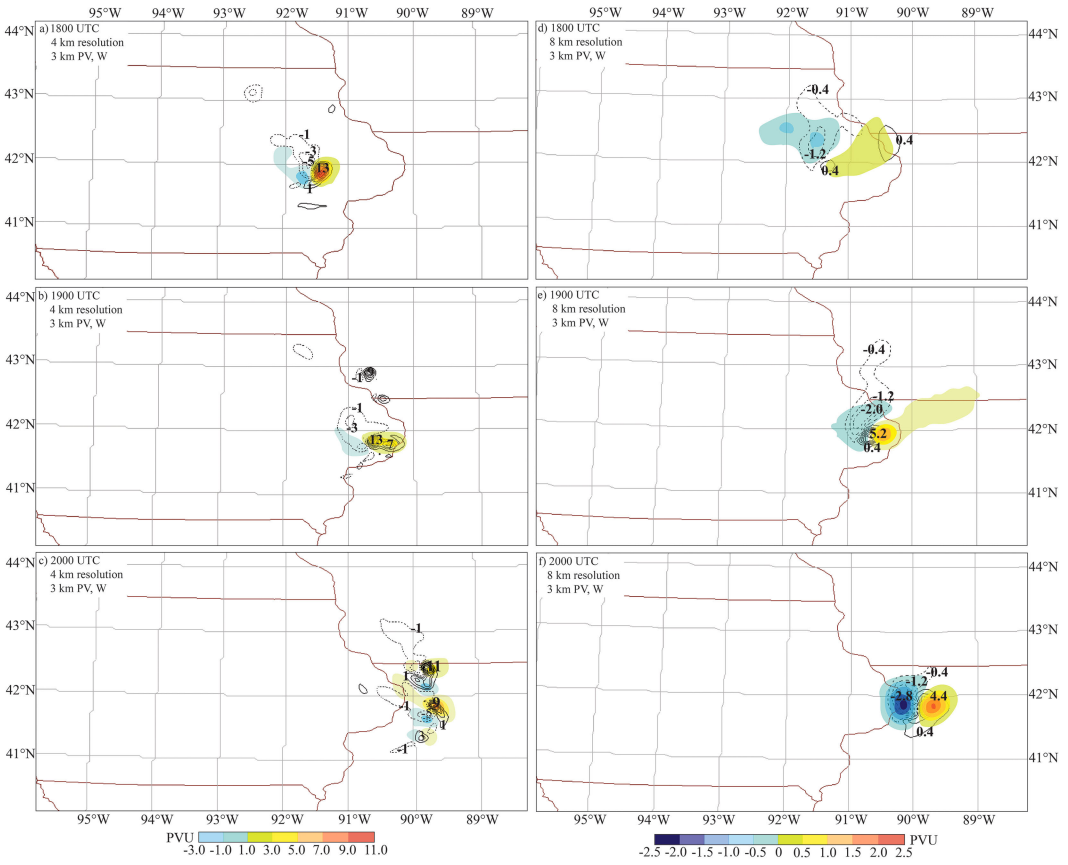

FIG. 8. Plan views of PV (color bar) and vertical velocity (m s^{-1}; contours, negative dashed) at 3-km altitude for (left) UWNMS-4 and (right) UWNMS-8 for (a),(d) 1800, (b),(e) 1900, and (c),(f) 2000 UTC 10 Aug 2020. In UWNMS-4, vertical velocity is contoured every 2 m s^{-1} and PV every 2 PVU, while in UWNMS-8 vertical velocity is contoured every 0.8 m s^{-1} and PV every 0.5 PVU.

layer exceeding 70 m s^{-1} near 12 km (Fig. 10a). The easterly outflow layer occurs at a lower altitude than in the UWNMS-4 at 1800 UTC. The zonal flow in the updraft (Fig. 10a) is much less easterly than in UWNMS-4 (Fig. 9a), reaching −3 m s^{-1} near 12 km (Fig. 10a). The axis of northerly flow in the lower troposphere lies between the westerly flow in the downdraft and weak westerly flow in the updraft (Figs. 10a–c) and between the PV dipoles (Fig. 10d). The negative PV anomaly coincides with the downdraft, and the positive PV anomaly coincides with the updraft (Figs. 10c,d). Over the next 2 h, the downdraft/updraft pair and PV dipole remained coherent in the UWNMS-8. The eastward movement of the PV dipole/northerly jet can explain the development of the trailing equatorward bulge of the gust front into southern Illinois (Fig. 2).

UWNMS-8 exhibited a development phase (1700 and 1800 UTC), mature phase (1900–2000 UTC), and decaying phase (2100 UTC) (Fig. 7a). This evolution is similar to the observed changes in the speed of propagation of the derecho, which was fastest during 1800–2100 UTC (Fig. 7a). The basic structure of a westerly midlevel inflow jet of ~25 m s^{-1} and a surface westerly maximum coinciding with the leading edge of the downdraft supports the idea that the speed of the westerly inflow jet is fundamentally related to the rate of eastward progression of the derecho.

The existence of a northerly jet is in agreement with the observations at DSM (Fig. 5b). Since the gust front arrived at DVN (90.58°W) at ~1900 UTC, we explore wind structure in the meridional plane at 90.58°W at 1900 and 1920 UTC (Fig. 11). A region of near-surface westerlies, ~50 km in meridional extent, is seen near 42°N, coinciding with the western half of the downdraft (Fig. 11a). This layer extends upward and poleward and is continuous with a layer of westerly flow to the north centered at ~6 km and exceeding ~20 m s^{-1} (Fig. 11a). A northerly jet maximizes at −18 m s^{-1} near 2 km and coincides with the center and eastern half of the downdraft (Fig. 11b). This region of northerly flow extends northward and upward from the gust front (Fig. 11b), lying between the westerlies to the north and weak zonal flow in the poleward-tilted updraft (Fig. 11a). In the UTLS, outflow jets extend primarily northward near 12 km from the updraft and also southward at 14 km (Fig. 11c).

Twenty minutes later, the region of southward flow exhibited a similar pattern (Figs. 11c,d), but the region of zonal flow exceeding 20 m s^{-1} has filled in the whole 1–5-km layer immediately behind the gust front (Fig. 11b). The axis of northerly flow associated with the gust front tilts northward

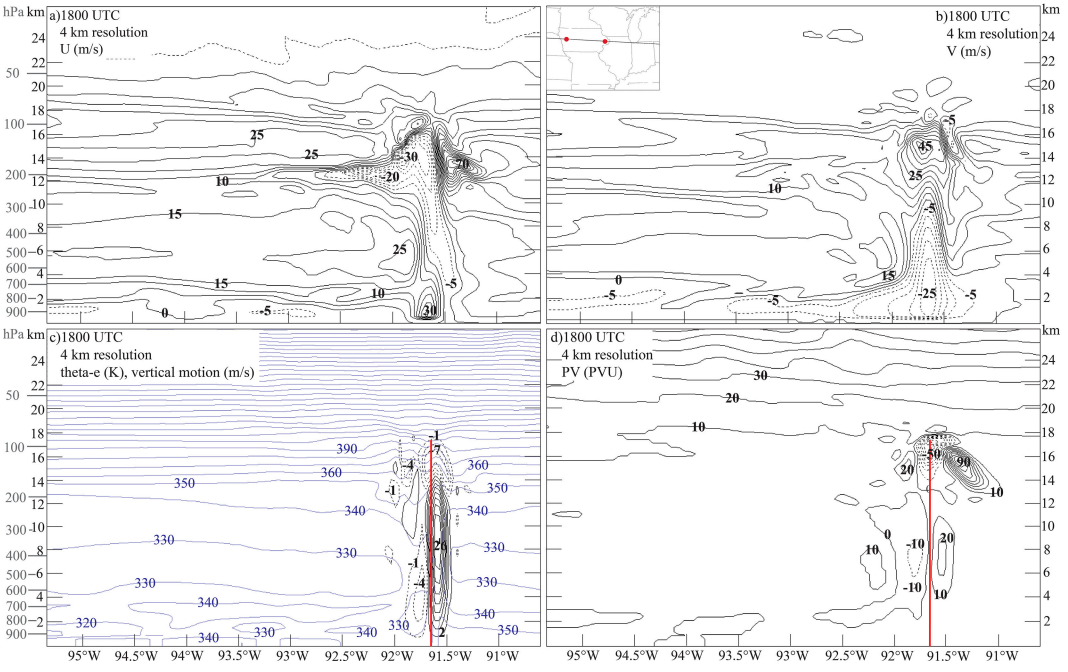

FIG. 9. Longitude–altitude sections in UWNMS-4 at 1800 UTC 10 Aug 2020 for (a) zonal wind (contour interval 5 m s^{-1}; negative dashed), (b) meridional wind (contour interval 5 m s^{-1}; negative dashed), (c) equivalent potential temperature (blue contours; interval 10 K) and vertical wind (contour interval 3 m s^{-1}; negative dashed), and (d) PV (contour interval 10 PVU; negative dashed). The vertical line in each panel indicates the longitude of maximum northerly flow in (b). The location of this section is shown in the inset of (b).

with height (Figs. 11b,d). It appears that air in the surface northerly jet is a blending of airstreams associated with the cyclonic member, the anticyclonic member, and the surface anticyclone to the north (Fig. 6f). Note the offset in altitude for outflow to the north (~12 km) and to the south (~14 km) (Fig. 11d).

Perspective views of speed isosurfaces show that the westerly inflow layer descends anticyclonically into the northerly outflow jet (Figs. 12a,b). The location of the northerly jet between the PV dipoles is shown in Fig. 12c. Since the negative PV dipole member is inertially unstable, this can contribute toward the acceleration of the northerly flow.

6. Depiction of derecho in HRRR analyses

a. Evolution of absolute vorticity at 150 and 700 hPa

During 8–10 August 2020, an upper-tropospheric ridge over the southeastern United States gradually weakened as a sequence of eastward-traveling troughs approached from the Gulf of Alaska (not shown). These troughs interacted with a ridge over the North Pacific in anticyclonic Rossby wave-breaking events, producing a filament of stratospheric air with high 150-hPa absolute vorticity extending southwestward across Colorado at 1600 UTC 10 August (Fig. 13a). Interrupting this filament of high absolute vorticity is a mesoscale absolute vorticity dipole, with positive member lying to the east and amplitude $\pm 10 \times 10^{-4}$ s^{-1} (Fig. 13a). Since isentropic density $\sigma = \rho(\partial z/\partial\theta) \sim 460$ kg K^{-1} m^{-2} near 150 hPa, from values in Fig. 3c, this corresponds to a PV dipole of amplitude $\sim \pm 2$ PVU. This UTLS PV dipole is observed to progress eastward with the derecho over the next three hours (Figs. 2 and 13a–d).

A similar eastward-progressing absolute vorticity dipole is seen at 700 hPa, with the positive member lying to the east (Figs. 13e–g). The dipole at 150 hPa lies ~50 km poleward of the dipole at 700 hPa, indicating a poleward tilt of the updraft. The zonal scale of each anomaly at 700 hPa is ~50 km, with a magnitude of $\sim \pm 10 \times 10^{-4}$ s^{-1}. Since $\sigma \sim 200$ kg K^{-1} m^{-2} near 700 hPa, this corresponds to an east–west PV dipole with the strength of $\sim \pm 5$ PVU.

The updraft at 150 hPa (Fig. 14a) coincides with the ~50-km scale zonal flow minimum (Fig. 6a) and with the negative absolute vorticity maximum (Fig. 13c). The updraft near 700 hPa occurs in an arc shape at the eastern end of the downdraft (Fig. 14b). The zonal scale of the anomalies at 700 hPa is ~50 km (Figs. 6f and 14b). The downdraft and negative PV anomaly at 700 hPa have a wider zonal scale (~100–150 km) than the updraft and positive PV anomaly (~50 km) (Figs. 13f and 14b). Maximum vertical velocities in the updraft are ~–40 Pa s^{-1} (~6 m s^{-1}) and ~10 Pa s^{-1} (~−1 m s^{-1}) in the downdraft (Fig. 14b).

The updraft in HRRR weakened from 1700 to 2000 UTC (Fig. 7a), whereas observations show more steady intensity (Fig. 2). The absolute vorticity dipole at 700 hPa is oriented east–west at 1700 UTC (Fig. 13e), but by 1800 UTC (Fig. 13f)

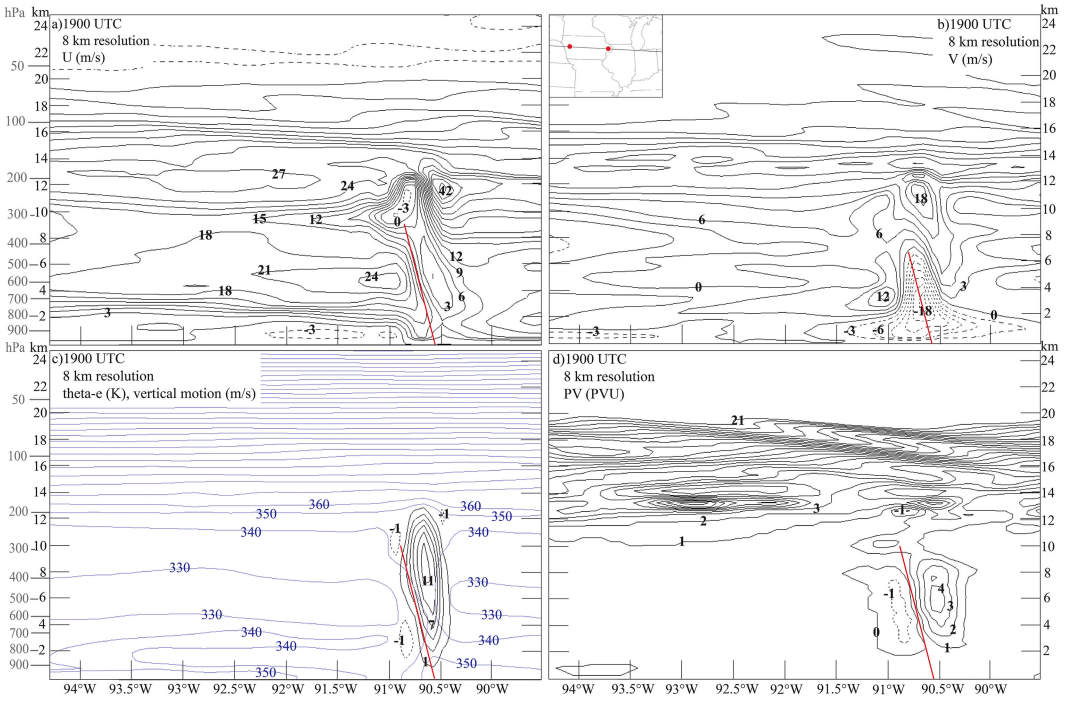

FIG. 10. Longitude–altitude sections in UWNMS-8 at 1900 UTC 10 Aug 2020 for (a) zonal wind (contour interval 3 m s^{-1}; negative dashed), (b) meridional wind (contour interval 3 m s^{-1}; negative dashed), (c) equivalent potential temperature (blue contours; interval 10 K) and vertical wind (contour interval 2 m s^{-1}; negative dashed), and (d) PV (contour interval 1 PVU; negative dashed). The tilted vertical line in each panel indicates the axis of maximum northerly wind.

the downdraft has become more diffuse and spread out to the south. This degradation of dipole structure in HRRR, compared with its persistence in the UWNMS-8, is consistent with the hypothesis that a stable dipole helps to maintain the strength of the derecho.

b. HRRR zonal and meridional sections

A movie of the longitude–altitude structure of zonal wind (Fig. S1) shows the evolution of the derecho in HRRR. In the early stages, the updraft was associated with moderate easterlies. The structure at 1800 UTC is now diagnosed in detail. Westerlies in the 700–400-hPa layer near 94°W extend eastward and downward to the surface near 92°W, with values exceeding ~35 m s^{-1} near 850 hPa, 92.3°W (Fig. 15a). A northerly jet occurs near the gust front, exceeding −20 m s^{-1} between 92.5° and 92°W in the 800–900-hPa layer (Fig. 15b). The midtropospheric westerly inflow jet curves equatorward as it descends in the downdraft (Figs. 15a–c). West of 92.5°W, a layer of easterly flow near 200 hPa (Fig. 15a) lies between the westerlies at 150 and 300 hPa (Figs. 6a,b).

Air in the westerly inflow layer splits, with one branch descending and curving southward, and the other rising into the upper troposphere and curving northward, where westerly flow exceeds 10 m s^{-1} (Figs. 15a,b). The downdraft coincides with the maximum in eastward flow (Figs. 15a,c), with values of ~5 Pa s^{-1} (−0.5 m s^{-1}) near 850 hPa. The downdraft (Fig. 15c), axis of maximum northerly flow (Fig. 15b), and westerly inflow layer (Fig. 15a) all tilt westward with height, with a slope of ~ −170 km (5 km)$^{-1}$ (elevation angle ~1.7°). The updraft ahead of the gust front (Fig. 15c) tilts westward with altitude, with slope of ~−30 km (8 km)$^{-1}$ (elevation angle ~15°). Updraft values exceed ~ −15 Pa s^{-1} (1.5 m s^{-1}) near 850 hPa and ~3 m s^{-1} near 400 hPa. Above ~650 hPa, the updraft coincides with weak westerly flow (Figs. 15a,c). Below 650 hPa, the updraft lies just to the east of the northerly jet maximum (Figs. 15b,c).

An east–west absolute vorticity dipole is found below 700 hPa, with values exceeding -5×10^{-4} s^{-1} and 20×10^{-4} s^{-1} (~–2.5 and 10 PVU) (Fig. 15d). The positive absolute vorticity region is located in the updraft, while the negative region is located in the downdraft (Figs. 15c,d). The maximum in northerly flow (Fig. 15b) tilts westward with altitude and lies along the zero contour separating the two absolute vorticity anomalies (Fig. 15d). This meridional jet is kinematically consistent with the east–west dipole in absolute vorticity. This mesobeta-scale PV dipole structure is distinct from the mesobeta cyclonic book-end vortex and mesogamma-scale MCVs. [Since the updraft also tilts poleward with altitude, the PV dipole in the UTLS maximizes ~50 km poleward of 42°N (Fig. 13c), such that this feature is not apparent in Fig. 15d.]

The pattern of strong westerlies which enters the downdraft descends from ~700 hPa (~3 km) to the surface (Fig. 15a). The updraft and downdraft near 800 hPa are ~50 km wide (Fig. 15c). The meridional breadth of the region of strong

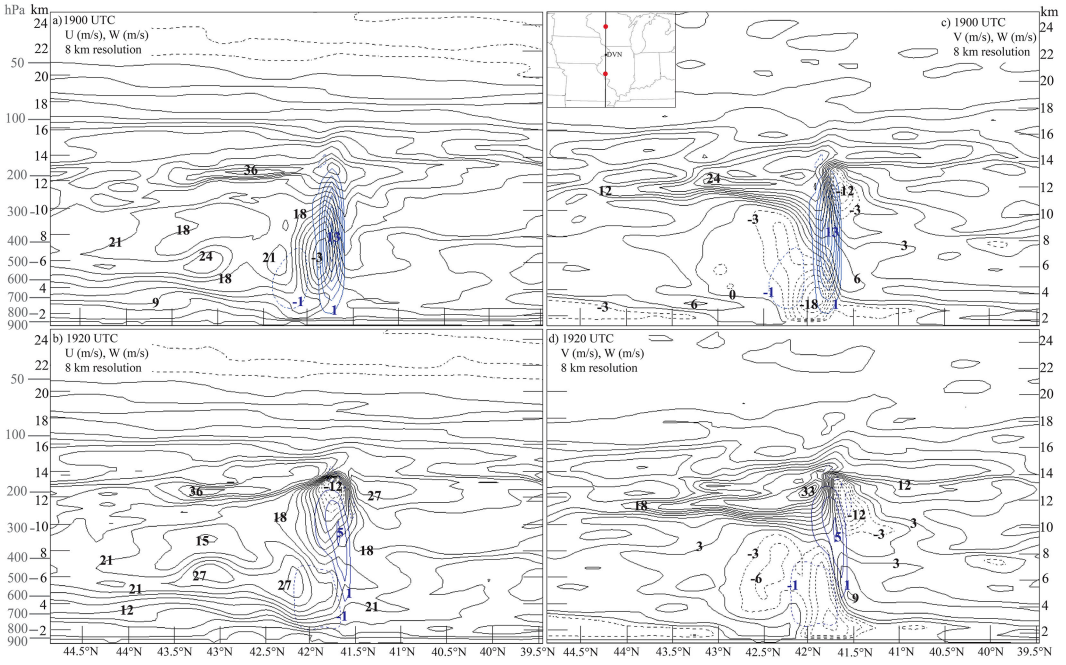

FIG. 11. Meridional sections along 90.58°W of UWNMS-8 (left) zonal wind and (right) meridional wind (black contours every 3 m s^{-1}; negative dashed), with vertical wind (blue contours every 2 m s^{-1}; negative dashed) at (top) 1900 and (bottom) 1920 UTC 10 Aug 2020. The view is toward the east, with the north to the left. The locations of the section ends (dots) are shown in the inset.

zonal winds is ~50 km at 92°W (Fig. 6e), but is ~150 km in the 700–850-hPa layer at 92.5°W (Fig. 16a). The meridional breadth of the updraft and downdraft (Figs. 16c,g) and of the absolute vorticity anomaly (Figs. 16d,h) in the lower troposphere is ~50 km.

The updraft and downdraft in an MCS are part of a pattern of gravity wave phase axes, which tilts westward with altitude (Lin 2007), with characteristic horizontal and vertical wavelengths L_x of ~ 200 km and L_z of ~ 12 km (Fig. 15c). These gravity waves may be related to the oscillations in pressure and wind speed seen at Des Moines after the passage of the gust front (Fig. 5a), which have a period of ~2 h. For a gravity wave to travel eastward 200 km in 2 h requires a zonal phase speed c of ~100 km h^{-1} or 28 m s^{-1}. Since this is the speed of propagation of the derecho, this suggests that there is a critical surface or steering level in the midtroposphere. In linear gravity wave theory, the relationship between pressure amplitude and wind amplitude is $P_o \rho c \sim V_o$. A pressure amplitude of 1.5 hPa (Fig. 5a) implies V_o of ~5 m s^{-1}, which is consistent with the variation in Fig. 16b.

A meridional slice at 92.5°W (Fig. 16a) shows that the westerly inflow jet below 650 hPa has a maximum of ~35 m s^{-1} near 42°N, which is continuous with westerlies in the

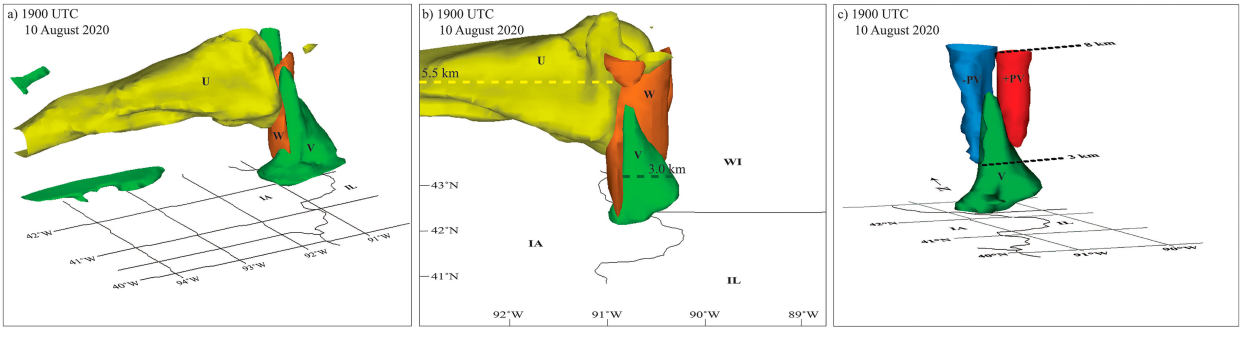

FIG. 12. Spatial relationship between the westerly inflow jet, the lower-tropospheric northerly jet, and the downdraft in UWNMS-8 at 1900 UTC 10 Aug 2020. Perspective views from (a) the southwest and (b) the south showing isosurfaces of zonal wind U (22 m s^{-1}; yellow), meridional wind V (−5 m s^{-1}; green), and vertical wind W (−0.8 m s^{-1}; orange) and (c) the southwest showing an isosurface of meridional wind V (−5 m s^{-1}; green), together with the −1 PVU (blue) and +2 PVU (red) isosurfaces. Selected altitudes are indicated in (b) and (c).

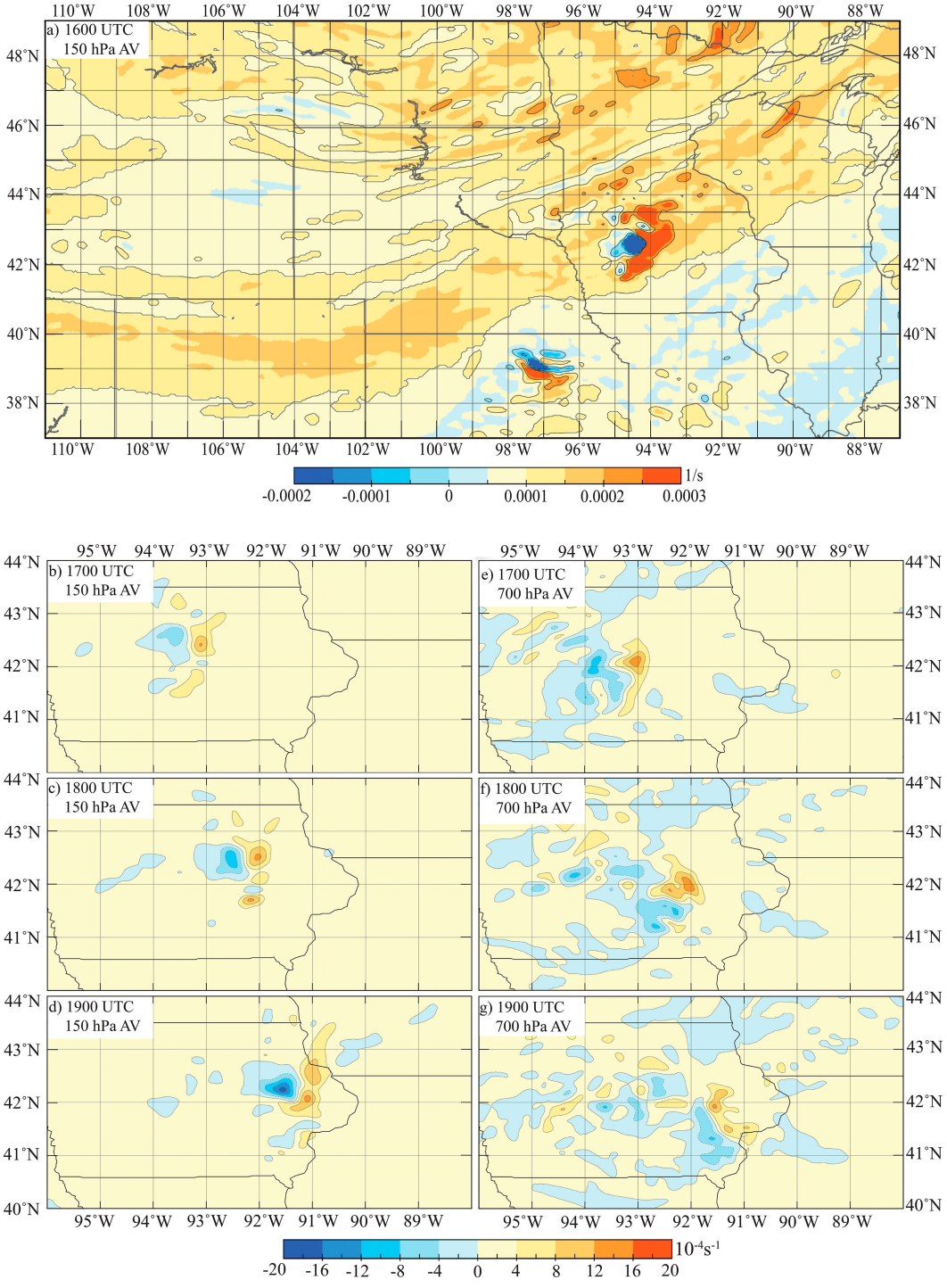

FIG. 13. HRRR absolute vorticity (color bar) at 150 hPa for (a) 1600, (b) 1700, (c) 1800, and (d) 1900 UTC 10 Aug 2020 and at 700 hPa for (e) 1700, (f) 1800, and (g) 1900 UTC. The color bar interval is 0.5×10^{-4} s^{-1} in (a) and 2×10^{-4} s^{-1} in (b)–(g).

800–700-hPa layer to the north (Figs. 6d and 16a). At 92°W, the "nose" of westerly flow is meridionally ~100 km wide (Fig. 16b). The layer of westerlies at 92.5°W coincides with northerly flow, with the layer descending as it moves southward (Figs. 16a–c). The nose of the derecho at 92°W contains a prominent northerly flow component (Figs. 16e,f).

At 92.5°W, the 600-hPa level separates the portion of the westerly inflow jet, which rises poleward into the upper

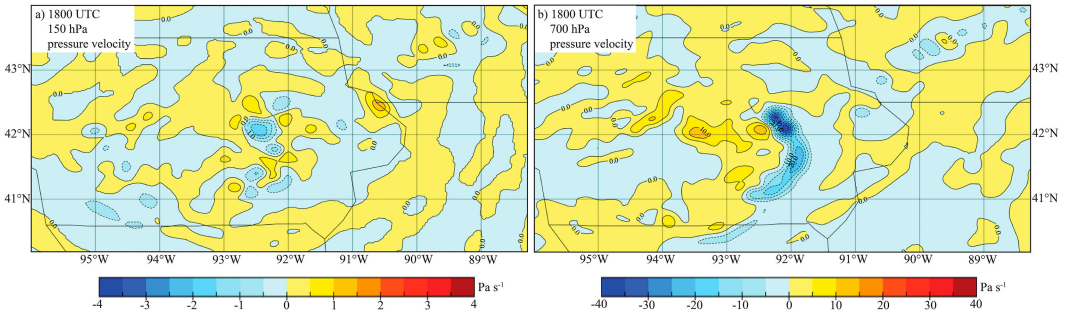

FIG. 14. HRRR pressure velocity (color bar; interval 0.5 Pa s^{-1}) at 1800 UTC 10 Aug 2020 for (a) 150 and (b) 700 hPa.

troposphere from that which descends equatorward in the downdraft (Figs. 16a–c). The meridional section of pressure velocity at 92°W (Fig. 16g) slices through the horseshoe-shaped, westward-tilting updraft, with a portion of the downdraft appearing in the middle near the surface, indicating that this is close to the gust front. At 92.5°W, the downdraft coincides with negative absolute vorticity in the lower troposphere (Figs. 16c,d), while near 92°W, positive absolute vorticity coincides with the updraft, which extends into the upper troposphere (Figs. 16g,h).

c. *Reynolds stresses*

Products of velocity components are useful for highlighting fundamental flow structures, estimating momentum fluxes, and relating them to the synoptic flow. Below the level of zero vertical wind, westerly momentum is transported southward (Figs. 17a,d). In the downdraft, westerly momentum (Figs. 17b,e) and northerly momentum (Figs. 17c,f) are transported downward within the derecho.

In the 500–700-hPa westerly inflow layer, $uv > 0$ (Fig. 17a), consistent with northward transport of westerly momentum associated with the approaching trough (Fig. 6c). In the UTLS, uv exhibits a quadrupole pattern in longitude–altitude associated with updraft outflow (Fig. 17a). The negative region near 200 hPa is consistent with southeasterly front-to-rear outflow and trailing stratiform precipitation (Houze et al. 1989). The positive region near 150 hPa is consistent with southwesterly outflow creating a layer of leading stratiform precipitation (Figs. 17a and 3a). At 92.5°W (Fig. 17d), one may see that this region of $uv > 0$ extends well to the north of the derecho.

Above ~600 hPa, there is upward transport of westerly momentum, where the upper half of the westerly inflow jet merges with the gust front updraft (Figs. 17b,e). This pattern of momentum flux divergence transports momentum away from the 700–500 westerly inflow jet, consistent with the deceleration observed in Fig. 15a. Near the top of the updraft at 150 hPa, the vertical momentum flux convergence near 92.2°W (Fig. 17b) is compatible with westerly acceleration in the outflow jet.

Below the zero vertical wind line near ~600 hPa, northerly and westerly momentum is transported downward in the downdraft, while above ~600 hPa, southerly and westerly momentum is transported upward in the updraft (Figs. 17c,e). These results are consistent with down-gradient transport from the midtropospheric westerly jet streak associated with the cyclone and from the northerly winds in the surface anticyclone.

d. *3D isosurfaces*

The westerly inflow jet curves anticyclonically as it descends and becomes the northerly outflow jet, as indicated by their spatial collocation viewed from the southwest and the south (Figs. 18a,b). This relationship is similar to that shown for UWNMS-8 in Figs. 12a and 12b, except the downdraft slopes more gently in HRRR. The pattern in the $v = -18$ m s^{-1} isosurface (Fig. 18b) shows the core outflow, plus the trailing speed maximum at the south edge of the gust front, as in Fig. 6f. This outflow jet lies between the absolute vorticity dipoles in HRRR (Fig. 18c), similar to UWNMS-8 (Fig. 12).

A view from the north reinforces these spatial relationships (Fig. 19). The region of westerlies associated with the upper-level cyclone is continuous with the westerly inflow jet and the northerly outflow jet, which occur to the east of the positive absolute vorticity anomaly (Fig. 19a). The meridional jet lies between the absolute vorticity dipoles (Fig. 19b). The westerly inflow jet and northerly jet blend, wrapping around the negative absolute vorticity anomaly (Fig. 19c).

7. Discussion

a. *Summary comparison*

All three numerical depictions show an east–west PV dipole structure in the mid- to lower troposphere, coincident with the updraft/downdraft pair, with a northerly jet between. HRRR maintained a continuous derecho-like structure in time, but lagged observed locations by ~80 km, with reduced zonal translation speed and weakening during 1700–2000 UTC. UWNMS-4 generated a derecho-like structure 2 h earlier than UWNMS-8, but the tilt of the updraft/downdraft was too weak, and rapid amplification was followed by a breakdown into MCVs. UWNMS-8 was slow to amplify but then maintained a coherent derecho-like structure for ~2 h, with amplitudes similar to HRRR, and exhibited a somewhat more realistic

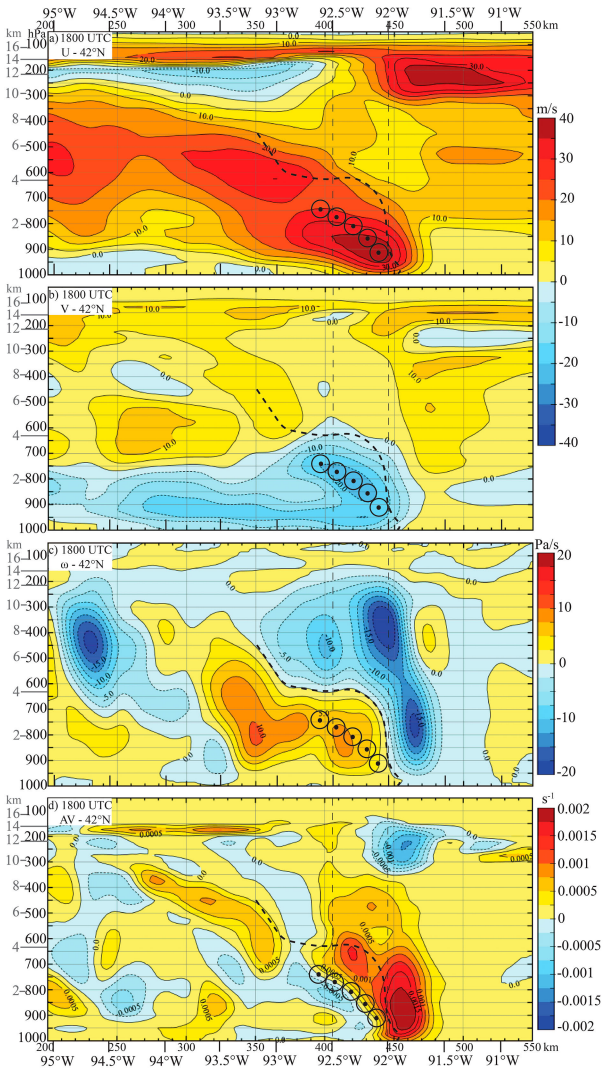

FIG. 15. Longitude–altitude sections at 42°N (looking north) of HRRR (a) zonal wind (color bar range; interval 5 m s^{-1}), (b) meridional wind (color bar; interval 5 m s^{-1}), (c) pressure velocity (color bar; interval 2.5 Pa s^{-1}), and (d) absolute vorticity (color bar; interval 0.000 25 s^{-1}) at 1800 UTC 10 Aug 2020. The zero vertical velocity line (heavy dashed) and locations of updrafts and downdrafts (arrows) in (c) are transposed onto (a), (b), and (d). The locus of southward flow in (b) is indicated with outward arrow symbols (⊙) and transposed onto (a), (c), and (d). Distance east of the center of the HRRR domain (km) is shown along the *x* axis. Pressure (hPa) and altitude (km; gray tick marks) are shown on the *y* axis.

westward tilt with height. The gentle slope of the downdraft in HRRR was more realistic.

b. *Role of steering level in the eastward progression of the derecho*

To remain coherent for several hours, the gust front cannot significantly outrun the downdraft. Under the steering level hypothesis, the speed of the gust front c should be related to a spatial average of the fastest portions of the westerly inflow layer U. The existence of such a steering level implies that there is a critical level where $c \sim U$. This may imply that the existence of a derecho depends on the existence of a midtropospheric westerly wind maximum, with moderate westerlies in the upper troposphere. This zonal wind profile, with shear ~25 m s^{-1} km^{-1}, is consistent with the proper combination of westward tilt with height and similar degree of outflow toward the northwest and northeast in the UTLS, as in the idealized modeling results of Weisman and Rotunno (2004).

Since the derecho speed was similar in UWNMS-8 and UWNMS-4, features such as a realistic tilt of the updraft/downdraft and a well-developed cold pool may be less important in determining storm motion than the zonal wind speed upstream in the 750–500-hPa layer. Note the existence of strong westerly flow in the 3–5-km layer to the north of the gust front (Figs. 11a,b and 16a). The movement of this "arm" of high-speed air associated with the upper-tropospheric cyclone guides the steering level of the derecho eastward.

c. *Role of steering level and comparison with breaking orographic gravity waves*

Peltier and Clark (1979), Lilly and Klemp (1979), and Durran and Klemp (1983) studied the saturation process of orographic gravity wave amplification to the point of turbulent breakdown, in which the downdraft brings high westerly wind speed air to the surface, followed by a hydraulic jump. The resulting region of stalled zonal flow in the updraft is similar to zonal wind sections in the UWNMS (Figs. 9a and 10a) and HRRR (Fig. 15a, Fig. S1). The zero wind surface is a critical surface for orographic gravity waves. In a derecho, the ~25 m s^{-1} zonal wind surface can be regarded as a critical surface for waves with $c \sim 25$ m s^{-1}, which grow by resonant amplification with the diabatic heating pattern traveling at the same rate. Critical surface theory can help explain both the observed emission of gravity waves from the storm and nonlinear saturation, or reaching a finite-amplitude quasi-steady state.

A westward tilt with height is required to achieve this configuration. In the case of the derecho, the forcing pattern is moving at the speed of the flow (Figs. 8 and 9 of Lin and Smith 1986). The speed of a phenomenon arising from a resonant instability is most likely to travel at the speed of the forcing agent. The derecho is somewhat like an orographic gravity wave propagating at the speed of the inflow layer. Instead of a hydraulic jump, however, there is vertical shear of the meridional wind, with a northerly flow maximum at the leading edge of the downdraft and a southerly component to the updraft.

d. *Mechanism of PV dipole formation*

In the mature phase, an east–west PV dipole forms in association with the tilted updraft/downdraft pair, with a northerly flow maximum between. Kinematically, a northerly jet implies that positive relative vorticity exists to its east and negative vorticity to its west. The formation of the horizontal PV dipole in the lower troposphere occurred in conjunction with

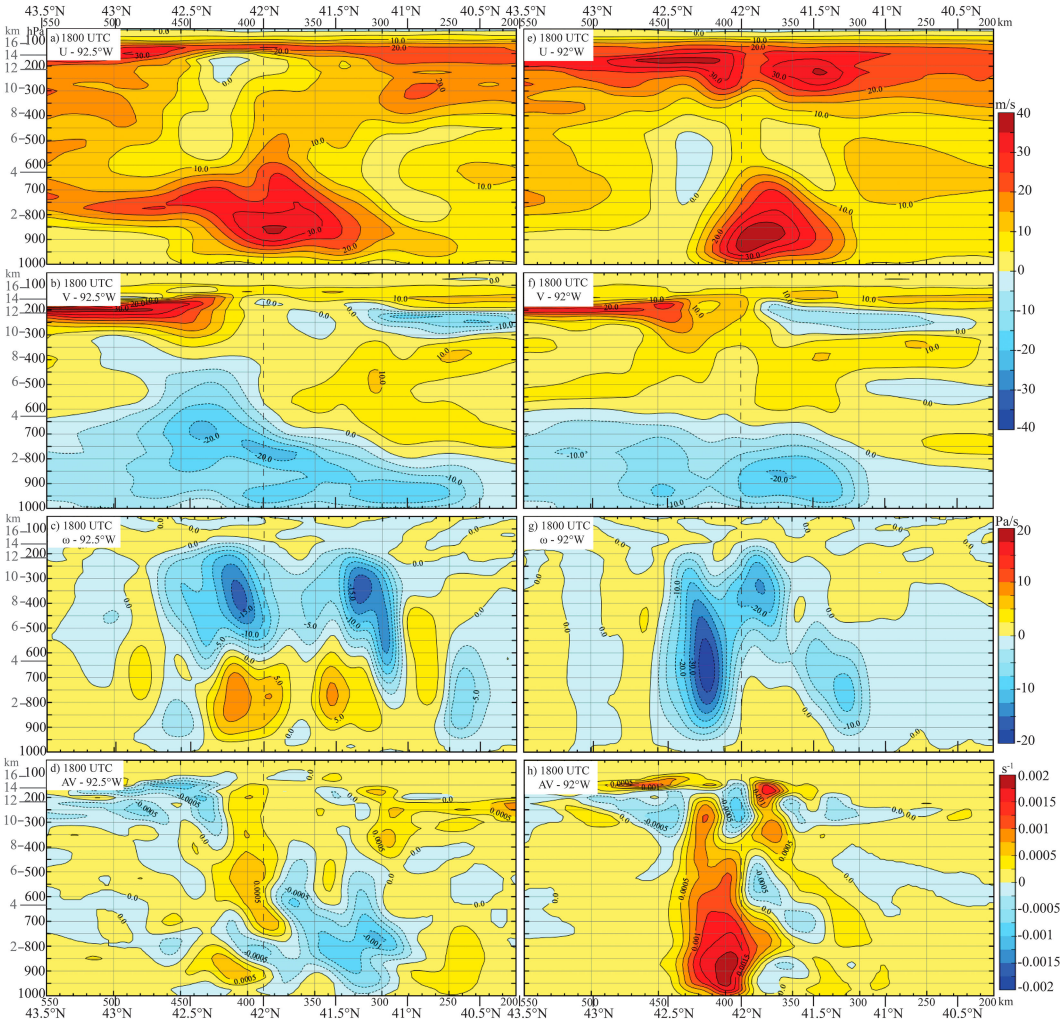

FIG. 16. Latitude–altitude sections (eastward view) at (left) 92.5°W and (right) 92°W of HRRR (a) zonal wind (color bar range; interval 5 m s^{-1}), (b) meridional wind (color bar; interval 5 m s^{-1}), (c) pressure velocity (color bar; interval 2.5 Pa s^{-1}), and (d) absolute vorticity (color bar; interval 0.000 25 s^{-1}) at 1800 UTC 10 Aug 2020. The dashed vertical line shows 42°N, the latitude of sections in Fig. 8. Distance north of the center of the HRRR domain is shown in kilometers. Pressure (hPa) and altitude (km; gray tick marks) are shown on the vertical axis.

the formation of an updraft and downdraft, which are caused by diabatic heating/cooling.

Evans et al. (2014) and Xu et al. (2015) emphasized the role of surface friction and tilting of near-surface horizontal vorticity as a generation mechanism for mesovortices in a derecho. However, the amplitude of the PV dipole diagnosed in the 10 August 2020 derecho increases upward from the surface and the PV dipole coincides with the westward-tilting updraft/downdraft pair (Figs. 9, 10, and 15d).

It is of interest to explore the effect of tilt on the diabatic stretching and tilting terms by considering the three progressively tilted structures shown in snapshots from the UWNMS-8 (Fig. 9), UWNMS-4 (Fig. 10), and HRRR (Fig. 15). The updraft and downdraft are most vertically oriented in the case of UWNMS-4 at 1800 UTC. The diabatic stretching tendency of P in (1) may be estimated as follows. Assuming that $w(\partial\theta/\partial z) \sim Q$ and $\partial\theta/\partial z = (\theta/T)[(\partial T/\partial z) + \Gamma_d]$, where Γ_d is the dry adiabatic lapse rate, an ambient moist adiabatic lapse rate $\partial T/\partial z \sim -6.5$ K km^{-1}, $\partial w/\partial z \sim 3\,m\,s^{-1}\,(2\,km)^{-1}$ km in the downdraft near 6 km (Fig. 9c), and $\zeta + f \sim -10^{-4}\,s^{-1}$, the diabatic stretching term in (1) is estimated to be ~ -3 PVU h^{-1}, perhaps sufficient to generate the negative PV anomaly in Fig. 9d. As an example from UWNMS-8, the updraft in Fig. 10c exhibits $\partial w/\partial z \sim 4\,m\,s^{-1}\,(2\,km)^{-1}$ near 4 km, with $\zeta + f \sim 2 \times 10^{-4}\,s^{-1}$, giving a diabatic stretching tendency of ~ 3 PVU h^{-1}, which may be adequate to generate the modeled positive PV anomaly in Fig. 10d.

As the tilt increases, the axes of maximum diabatic stretching tendency shift westward and underneath relative to the updraft and downdraft axes. This may be seen by estimating the diabatic stretching tendency in (2) for HRRR at 800 hPa, 92.5°W (just below the downdraft maximum), in the updraft

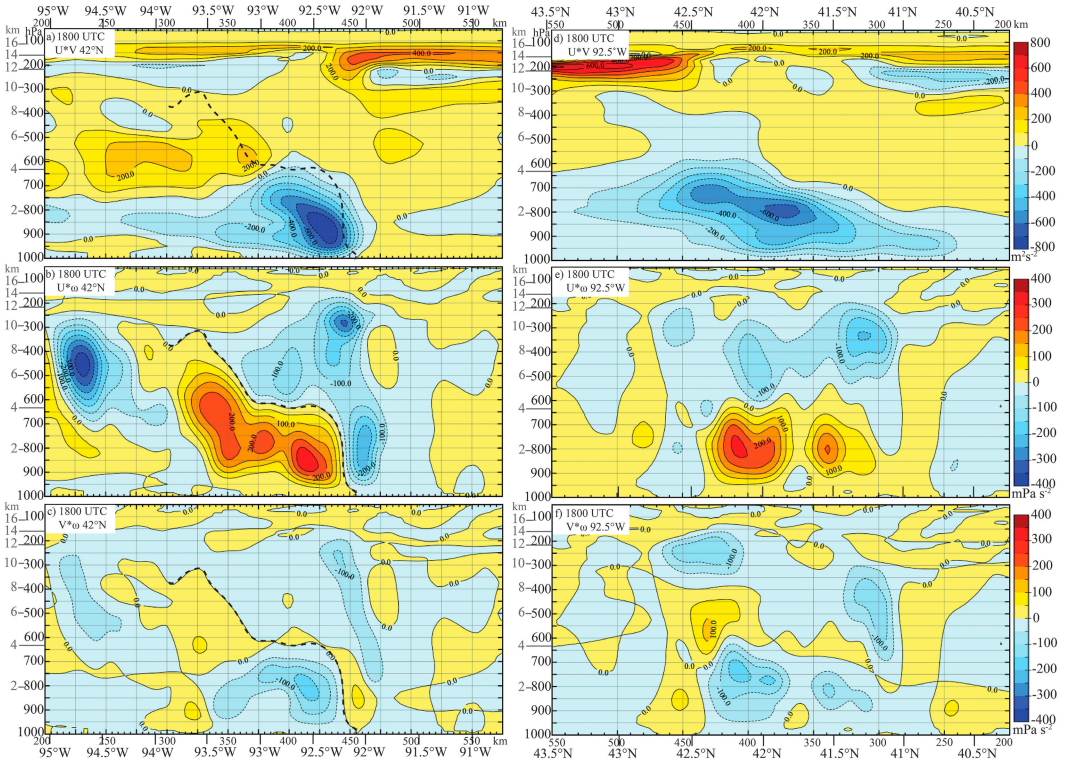

FIG. 17. Reynolds stresses (top) uv (color bar; interval 100 m^2 s^{-2}), (middle) $u\omega$ (color bar; interval 50 m Pa s^{-2}), and (bottom) $v\omega$ (color bar; interval 50 m Pa s^{-2}) in HRRR (a)–(c) for longitude–altitude sections at 42°N looking north and (d)–(f) for a latitude–altitude section at 92.5°W looking east. The zero vertical wind line in Fig. 15c) is transposed onto (a)–(c). At left, both longitude and distance (km) east of the center of the HRRR domain are shown. At right, both latitude and distance north of the center of the HRRR domain are shown. Pressure (hPa) and altitude (km; gray tick marks) are shown on the vertical axis.

near 850 hPa, 91.8°W (Fig. 15c), and near 650 hPa, 92.3°W (below the updraft maximum). Taking $\partial\omega/\partial p \sim 5$ Pa s^{-1}/ -100 hPa and $\zeta + f \sim 10^{-4}$ s^{-1} in the westerly inflow jet below the downdraft maximum, vortex stretching Pa s^{-1} gives $\sim -2 \times 10^{-4}$ s^{-1} h^{-1}. Taking $\partial\omega/\partial p \sim -10$ Pa s^{-1}/ -100 hPa in the updraft, vortex stretching gives $\sim 4 \times 10^{-4}$ s^{-1} h^{-1}, while taking $\partial\omega/\partial p \sim -15$ Pa s^{-1}/ -200 hPa below the updraft maximum, vortex stretching gives $\sim 3 \times 10^{-4}$ s^{-1} h^{-1}, comparable with absolute vorticity magnitudes in Fig. 15d. Note that the positive absolute vorticity maximum tilts westward such that it coincides with the zero wind line (Fig. 15d), where the vertical gradient in pressure velocity (Fig. 15c), hence diabatic stretching, is large. This westward and downward displacement in diabatic tilting tendency is a direct result of increasing tilt (Fig. 20).

Since the gradients in the diabatic tilting terms maximize between the PV dipoles, they cannot strengthen the dipole. In the case of weak tilt, both diabatic tilting terms contribute toward negative PV tendency, maximizing along the axis of northerly flow, in quadrature with the PV anomalies. In the case of stronger tilt, products of gradients yield fine-scale patterns between the PV anomalies, with $(\partial w/\partial y)(\partial u/\partial z)$ in (2) causing positive tendency to the east of the negative PV anomaly and negative tendency to the west of the positive PV anomaly, while $-[(\partial w/\partial x)(\partial v/\partial z)]$ causes the opposite pattern,

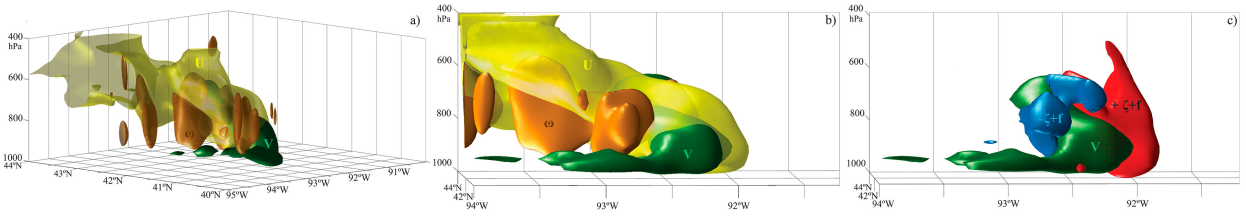

FIG. 18. HRRR 3D isosurfaces for 1800 UTC 10 Aug 2020 of (a) $u = 23$ m s^{-1} (yellow), $v = -18$ m s^{-1} (green), and $\omega = 6$ Pa s^{-1} (orange) viewed obliquely from the southwest; (b) as in (a), but viewed from the south; and (c) $v = -18$ m s^{-1} (green), $\zeta + f = 10 \times 10^{-4}$ s^{-1} (red), and $\zeta + f = -7 \times 10^{-4}$ s^{-1} (blue) viewed from the south.

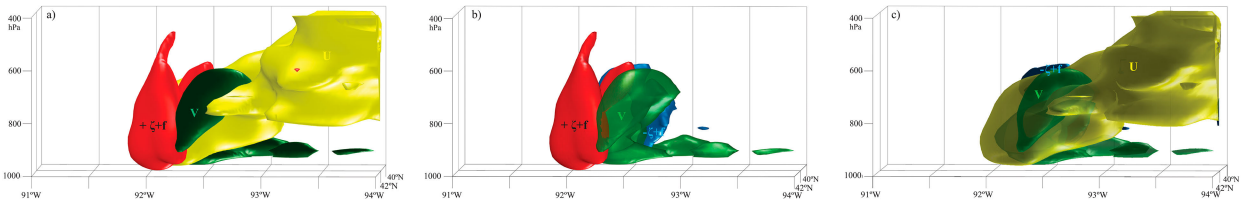

FIG. 19. HRRR 3D isosurfaces for 1800 UTC 10 Aug 2020 viewed from the north of (a) $u = 23$ m s^{-1} (yellow), $v = -18$ m s^{-1} (green), and $\zeta + f = 10 \times 10^{-4}$ s^{-1} (red), (b) $v = -18$ m s^{-1} (green), $\zeta + f = 10 \times 10^{-4}$ s^{-1} (red), and $\zeta + f = -7 \times 10^{-4}$ s^{-1} (blue), and (c) $u = 23$ m s^{-1} (yellow), $v = -18$ m s^{-1} (green), and $\zeta + f = -7 \times 10^{-4}$ s^{-1} (blue).

tending to cancel the other out. At the three locations described above (Fig. 15), $\partial\omega/\partial x \sim 0 \sim \partial\omega/\partial y$, so the diabatic tilting term is expected to be small. This analysis suggests that the diabatic stretching term is primarily responsible for generating the PV dipole. The generation and maintenance of the PV dipole may facilitate the coherence and longevity of a derecho.

The westerly inflow layer which curves anticyclonically in the downdraft and the gust front inflow layer which curves cyclonically in the updraft can be understood in terms of the horizontal momentum equations following the motion:

$$\frac{du}{dt} = fv - \frac{1}{\rho}\frac{\partial p}{\partial x}, \tag{3a}$$

$$\frac{dv}{dt} = -fu - \frac{1}{\rho}\frac{\partial p}{\partial y}. \tag{3b}$$

As air in the westerly inflow layer travels eastward, the northward pressure gradient force diminishes as it descends, such that northerly acceleration occurs [(3b)]. An increase in the westward pressure gradient force and the Coriolis torque on northerly flow causes the zonal flow to decelerate [(3a)], yielding anticyclonic vorticity in the downdraft. As air in the gust front inflow layer ascends, an increasing northward pressure gradient force and Coriolis torque on easterly flow cause southerly acceleration [(3b)], yielding cyclonic vorticity in the updraft. The existence of a stagnation point at the east end of the westerly inflow jet in the midtroposphere implies the existence of a mesohigh, which steers the westerly inflow layer southward as it descends and the front-to-rear flow northward as it ascends. As the westerly inflow jet curves around the anticyclonic member, angular momentum decreases radially outward, consistent with inertial instability, where air with high angular momentum diverges outward, creating the northerly outflow jet.

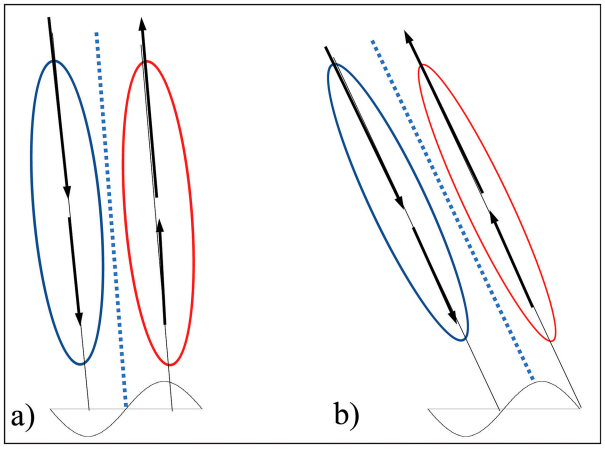

FIG. 20. Idealized diagram showing the maxima in diabatic stretching tendency for (a) weak tilt and (b) strong tilt. The downdraft (convergent arrows) coincides with negative PV anomaly (blue), and the updraft (divergent arrows) coincides with positive PV anomaly (red), with a northerly jet between (dotted blue axis). With increasing tilt, the maxima in diabatic stretching tendency, as indicated by the curve below each diagram, are displaced westward and downward relative to the updraft and the downdraft.

8. Conclusions

The Iowa derecho of 10 August 2020 was characterized by westerly winds exceeding 30 m s^{-1} in a ~100-km-wide swath through central Iowa, developing an equatorward expansion as it traveled eastward, forming a comma echo. When the gust front reached DSM at 1600 UTC, the temperature dropped 11 K in 10 min, due to the advection of low values of θ_e by the downdraft, replacing the previous boundary layer air. The pressure rose initially by ~5 hPa and remained elevated for several hours during the passage of the mesoanticyclone. The arrival of the gust front was characterized by an abrupt shift to northerly flow and a rapid increase in speed (Fig. 5b). The speed of the flow in the 500–750-hPa westerly inflow layer upstream of the gust front is similar to the speed of propagation of the derecho. The westerly inflow layer is a southward extension of a region of high wind speed (jet streak) associated with the approaching synoptic trough. As pointed out by Hinrichs (1888), there is a significant northerly aspect to the surface outflow. Below 850 hPa, the northerly jet between the updraft/downdraft and the PV dipole exists proximal to the southeastern flank of the lower-tropospheric anticyclone.

When the updraft/downdraft pair strengthened, an east–west PV dipole formed primarily by diabatic stretching and propagated eastward with the derecho, with the northerly outflow jet creating a comma radar echo pattern. These structures in HRRR and UWNMS confirm that the observed northerly jet at Des Moines implies an east–west PV dipole in the lower troposphere.

In a derecho, the positive PV anomaly extends to higher altitudes than the negative PV anomaly, with westerly inflow

above 5 km contributing to the updraft and the negative PV anomaly beginning near the top of the downdraft, which is confined below 5 km. The inertially unstable property of the negative PV member may help facilitate northerly acceleration, promoting the equatorward bulge of the radar echo.

The fundamental structure of a westward-tilted PV dipole may be on a continuum, which includes the more upright structure in a mature MCS studied by Fritsch et al. (1994) and Jiang and Raymond (1995), where a mesoscale warm-core vortex (positive PV anomaly) in the latent heat-driven updraft maximizes in the midtroposphere, with a shallow anticyclone (negative PV anomaly) near the surface. With a westerly inflow layer, a tilted structure forms with the near-surface PV anomaly maximizing in the midtroposphere. If the cold pool is poorly developed, such as in UWNMS-4 at 1800 UTC (Fig. 9), the PV dipole extends through most of the depth of the troposphere, with the negative member maximizing at the level of westerly inflow where the vertical wind diverges (Figs. 9a,c,d). With a more developed cold pool, such as in UWNMS-8 at 1900 UTC (Fig. 10), the PV dipole maximizes at a lower altitude. Finally, in HRRR (Fig. 15), the slope of the downdraft is much more gentle and the negative member of the PV dipole tilts more and maximizes at a still lower altitude.

These results can be interpreted in the context of the idealized study by Weisman and Rotunno (2004). The midtropospheric westerly inflow layer was shown to be associated with a region of westerlies extending southward from the approaching cyclone. This jet streak provides a steering level or critical level for the derecho, which can help amplify the structure. In this present case, the wind profile is most similar to their case with shallow shear at 20 m s^{-1}/5 km and constant westerlies above. The formation of a horizontal PV dipole may contribute to strengthening and stabilizing the self-perpetuating structure of a derecho. Since the speed of propagation of the derecho was very similar in HRRR, UWNMS-4, and UWNMS-8, despite differing strengths and structures, this supports the hypothesis that the speed of the derecho is controlled by a steering level flow which is related to the jet streak in the synoptic-scale cyclone.

Acknowledgments. The authors would like to acknowledge support from NSF Grant AGS-1947658. We thank Pete Pokrandt for help with converting the HRRR grid to local latitude/longitude. We are grateful to the reviewers who provided many helpful comments, especially Editor Russ Schumacher's suggestion of using HRRR data.

Data availability statement. Composite radar files are available from https://mesonet.agron.iastate.edu/current/mcview.phtml?prod=comprad&java=script&mode=archive&frames. Surface meteorological observations are available from https://mesonet.agron.iastate.edu/request/asos/1min.phtml#. The Davenport, Iowa, sounding is available from https://www.spc.noaa.gov/exper/archive/event.php?date=20200810. Observations for creating the surface station plot are available from https://rda.ucar.edu/. The NOAA NEXRAD-II *GOES-16* images and lightning data are available from https://www.ncdc.noaa.gov/wct/. NOAA High-Resolution Rapid Refresh (HRRR) model was last accessed on 15 July 2023 from https://registry.opendata.aws/noaa-hrrr-pds. UWNMS images may be reproduced from the VIS5D files of the simulations, which are stored on a dedicated computer in the AOS Department at the UW–Madison, available from the authors.

REFERENCES

Adams-Selin, R. D., 2020: Impact of convectively generated low-frequency gravity waves on evolution of mesoscale convective systems. *J. Atmos. Sci.*, **77**, 3441–3460, https://doi.org/10.1175/JAS-D-19-0250.1.

——, and R. H. Johnson, 2013: Examination of gravity waves associated with the 13 March 2003 bow echo. *Mon. Wea. Rev.*, **141**, 3735–3756, https://doi.org/10.1175/MWR-D-12-00343.1.

Andrews, D. G., J. R. Holton, and C. B. Leovy, 1987: *Middle Atmosphere Dynamics*. Academic Press, 489 pp.

Atkins, N. T., and M. St. Laurent, 2009: Bow echo mesovortices. Part I: Processes that influence their damaging potential. *Mon. Wea. Rev.*, **137**, 1497–1513, https://doi.org/10.1175/2008MWR2649.1.

Bretherton, C. S., and P. K. Smolarkiewicz, 1989: Gravity waves, compensating subsidence and detrainment around cumulus clouds. *J. Atmos. Sci.*, **46**, 740–759, https://doi.org/10.1175/1520-0469(1989)046<0740:GWCSAD>2.0.CO;2.

Campbell, M. A., A. E. Cohen, M. C. Coniglio, A. R. Dean, S. F. Corfidi, S. J. Corfidi, and C. M. Mead, 2017: Structure and motion of severe-wind-producing mesoscale convective systems and derechos in relation to the mean wind. *Wea. Forecasting*, **32**, 423–439, https://doi.org/10.1175/WAF-D-16-0060.1.

Chagnon, J. M., and S. L. Gray, 2009: Horizontal potential vorticity dipoles on the convective storm scale. *Quart. J. Roy. Meteor. Soc.*, **135**, 1392–1408, https://doi.org/10.1002/qj.468.

Chicago Weather Forecast Office, 2020: August 10, 2020: Corn Belt Derecho. Accessed 1 June 2023, https://www.weather.gov/lot/2020aug10.

Coniglio, M. C., and D. J. Stensrud, 2004: Interpreting the climatology of derechos. *Wea. Forecasting*, **19**, 595–605, https://doi.org/10.1175/1520-0434(2004)019<0595:ITCOD>2.0.CO;2.

——, ——, and M. B. Richman, 2004: An observational study of derecho-producing convective systems. *Wea. Forecasting*, **19**, 320–337, https://doi.org/10.1175/1520-0434(2004)019<0320:AOSODC>2.0.CO;2.

Corfidi, S. F., J. H. Merritt, and J. M. Fritsch, 1996: Predicting the movement of mesoscale convective complexes. *Wea. Forecasting*, **11**, 41–46, https://doi.org/10.1175/1520-0434(1996)011<0041:PTMOMC>2.0.CO;2.

——, M. C. Coniglio, A. E. Cohen, and C. M. Mead, 2016: A proposed revision to the definition of "derecho". *Bull. Amer. Meteor. Soc.*, **97**, 935–949, https://doi.org/10.1175/BAMS-D-14-00254.1.

Davies-Jones, R., 1984: Streamwise vorticity: The origin of updraft rotation in supercell storms. *J. Atmos. Sci.*, **41**, 2991–3006, https://doi.org/10.1175/1520-0469(1984)041<2991:SVTOOU>2.0.CO;2.

Davis, C. A., and T. J. Galarneau Jr., 2009: The vertical structure of mesoscale convective vortices. *J. Atmos. Sci.*, **66**, 686–704, https://doi.org/10.1175/2008JAS2819.1.

Dowell, D. C., and Coauthors, 2022: The High-Resolution Rapid Refresh (HRRR): An hourly updating convection-allowing

forecast model. Part I: Motivation and system description. *Wea. Forecasting*, **37**, 1371–1395, https://doi.org/10.1175/WAF-D-21-0151.1.

Durran, D. R., and J. B. Klemp, 1983: A compressible model for the simulation of moist mountain waves. *Mon. Wea. Rev.*, **111**, 2341–2361, https://doi.org/10.1175/1520-0493(1983)111<2341:ACMFTS>2.0.CO;2.

Evans, C., M. L. Weisman, and L. F. Bosart, 2014: Development of an intense, warm-core mesoscale vortex associated with the 8 May 2009 "super derecho" convective event. *J. Atmos. Sci.*, **71**, 1218–1240, https://doi.org/10.1175/JAS-D-13-0167.1.

Evans, J. S., and C. A. Doswell III, 2001: Examination of derecho environments using proximity soundings. *Wea. Forecasting*, **16**, 329–342, https://doi.org/10.1175/1520-0434(2001)016<0329:EODEUP>2.0.CO;2.

Fovell, R. G., G. L. Mullendore, and S.-H. Kim, 2006: Discrete propagation in numerically simulated nocturnal squall lines. *Mon. Wea. Rev.*, **134**, 3735–3752, https://doi.org/10.1175/MWR3268.1.

Fritsch, J. M., J. D. Murphy, and J. S. Kain, 1994: Warm core vortex amplification over land. *J. Atmos. Sci.*, **51**, 1780–1807, https://doi.org/10.1175/1520-0469(1994)051<1780:WCVAOL>2.0.CO;2.

Guastini, C. T., and L. F. Bosart, 2016: Analysis of a progressive derecho climatology and associated formation environments. *Mon. Wea. Rev.*, **144**, 1363–1382, https://doi.org/10.1175/MWR-D-15-0256.1.

Harvey, B., J. Methven, C. Sanchez, and A. Schäfler, 2020: Diabatic generation of negative potential vorticity and its impact on the North Atlantic jet stream. *Quart. J. Roy. Meteor. Soc.*, **146**, 1477–1497, https://doi.org/10.1002/qj.3747.

Hashino, T., and G. J. Tripoli, 2007: The Spectral Ice Habit Prediction System (SHIPS), Part I: Model description and simulation of the vapor deposition process. *J. Atmos. Sci.*, **64**, 2210–2237, https://doi.org/10.1175/JAS3963.1.

——, and ——, 2011: The Spectral Ice Habit Prediction System (SHIPS), Part IV: Box model simulations of the habit-dependent aggregation process. *J. Atmos. Sci.*, **68**, 1142–1161, https://doi.org/10.1175/2011JAS3667.1.

Haynes, P. H., and M. E. McIntyre, 1990: On the conservation and impermeability theorems for potential vorticity. *J. Atmos. Sci.*, **47**, 2021–2031, https://doi.org/10.1175/1520-0469(1990)047<2021:OTCAIT>2.0.CO;2.

Hernandez-Duenas, G., L. M. Smith, and S. N. Stechmann, 2014: Investigation of Boussinesq dynamics using intermediate models based on wave–vertical interactions. *J. Fluid Mech.*, **747**, 247–287, https://doi.org/10.1017/jfm.2014.138.

Hinrichs, G., 1888: Tornadoes and derechos. *Amer. Meteor. J.*, **5**, 341–349.

Hitchman, M. H., and S. M. Rowe, 2017: On the similarity of lower stratospheric potential vorticity dipoles above tropical and midlatitude deep convection. *J. Atmos. Sci.*, **74**, 2593–2613, https://doi.org/10.1175/JAS-D-16-0239.1.

——, and ——, 2019: On the structure and formation of UTLS PV dipole/jetlets in tropical cyclones by convective momentum surge. *Mon. Wea. Rev.*, **147**, 4107–4125, https://doi.org/10.1175/MWR-D-18-0232.1.

——, and ——, 2021: On the formation of tropopause folds and constituent gradient enhancement near westerly jets. *J. Atmos. Sci.*, **78**, 2057–2074, https://doi.org/10.1175/JAS-D-20-0013.1.

Holton, J. R., and G. J. Hakim, 2013: *An Introduction to Dynamic Meteorology*. 5th ed. Elsevier Science, 532 pp.

Houze, R. A., Jr., S. A. Rutledge, M. I. Biggerstaff, and B. F. Smull, 1989: Interpretation of Doppler weather radar displays of midlatitude mesoscale convective systems. *Bull. Amer. Meteor. Soc.*, **70**, 608–619, https://doi.org/10.1175/1520-0477(1989)070<0608:IODWRD>2.0.CO;2.

Jiang, H., and D. J. Raymond, 1995: Simulation of a mature mesoscale convective system using a nonlinear balance model. *J. Atmos. Sci.*, **52**, 161–175, https://doi.org/10.1175/1520-0469(1995)052<0161:SOAMMC>2.0.CO;2.

Johns, R. H., and W. D. Hirt, 1987: Derechos: Widespread convectively induced windstorms. *Wea. Forecasting*, **2**, 32–49, https://doi.org/10.1175/1520-0434(1987)002<0032:DWCIW>2.0.CO;2.

Lane, T. P., and F. Zhang, 2011: Coupling between gravity waves and tropical convection at mesoscales. *J. Atmos. Sci.*, **68**, 2582–2598, https://doi.org/10.1175/2011JAS3577.1.

Lilly, D. K., and J. B. Klemp, 1979: The effects of terrain shape on nonlinear hydrostatic mountain waves. *J. Fluid Mech.*, **95**, 241–261, https://doi.org/10.1017/S0022112079001452.

Lin, Y.-L., 2007: *Mesoscale Dynamics*. Cambridge University Press, 630 pp.

——, and R. B. Smith, 1986: Transient dynamics of airflow near a local heat source. *J. Atmos. Sci.*, **43**, 40–49, https://doi.org/10.1175/1520-0469(1986)043<0040:TDOANA>2.0.CO;2.

Mahoney, K. M., G. M. Lackmann, and M. D. Parker, 2009: The role of momentum transport in the motion of a quasi-idealized mesoscale convective system. *Mon. Wea. Rev.*, **137**, 3316–3338, https://doi.org/10.1175/2009MWR2895.1.

Markowski, P., and Y. Richardson, 2010: *Mesoscale Meteorology in Midlatitudes*. John Wiley and Sons, 407 pp.

Montgomery, M. T., M. E. Nicholls, T. A. Cram, and A. B. Saunders, 2006: A vortical hot tower route to tropical cyclogenesis. *J. Atmos. Sci.*, **63**, 355–386, https://doi.org/10.1175/JAS3604.1.

Muraki, D. J., and C. Snyder, 2007: Vortex dipoles for surface quasigeostrophic models. *J. Atmos. Sci.*, **64**, 2961–2967, https://doi.org/10.1175/JAS3958.1.

Oertel, A., M. Boettcher, H. Joos, M. Sprenger, and H. Wernli, 2020: Potential vorticity structure of embedded convection in a warm conveyor belt and its relevance for large-scale dynamics. *Wea. Climate Dyn.*, **1**, 127–153, https://doi.org/10.5194/wcd-1-127-2020.

Pandya, R. E., D. R. Durran, and M. L. Weisman, 2000: The influence of convective thermal forcing on the three-dimensional circulation around squall lines. *J. Atmos. Sci.*, **57**, 29–45, https://doi.org/10.1175/1520-0469(2000)057<0029:TIOCTF>2.0.CO;2.

Peltier, W. R., and T. L. Clark, 1979: The evolution and stability of finite-amplitude mountain waves. Part II. Surface wave drag and severe downslope windstorms. *J. Atmos. Sci.*, **36**, 1498–1529, https://doi.org/10.1175/1520-0469(1979)036<1498:TEASOF>2.0.CO;2.

Plougonven, R., and F. Zhang, 2014: Internal gravity waves from atmospheric jets and fronts. *Rev. Geophys.*, **52**, 33–76, https://doi.org/10.1002/2012RG000419.

Prince, K. C., and C. Evans, 2022: Convectively generated negative potential vorticity enhancing the jet stream through an inverse energy cascade during the extratropical transition of Hurricane Irma. *J. Atmos. Sci.*, **79**, 2901–2918, https://doi.org/10.1175/JAS-D-22-0094.1.

Przybylinski, R. W., 1995: The bow echo: Observations, numerical simulations, and severe weather detection methods. *Wea. Forecasting*, **10**, 203–218, https://doi.org/10.1175/1520-0434(1995)010<0203:TBEONS>2.0.CO;2.

Raymond, D. J., and H. Jiang, 1990: A theory for long-lived mesoscale convective systems. *J. Atmos. Sci.*, **47**, 3067–3077, https://doi.org/10.1175/1520-0469(1990)047<3067:ATFLLM>2.0.CO;2.

Rocha, C. B., G. L. Wagner, and W. R. Young, 2018: Stimulated generation: Extraction of energy from balanced flow by near-inertial waves. *J. Fluid Mech.*, **847**, 417–451, https://doi.org/10.1017/jfm.2018.308.

Rotunno, R., J. B. Klemp, and M. L. Weisman, 1988: A theory for strong, long-lived squall lines. *J. Atmos. Sci.*, **45**, 463–485, https://doi.org/10.1175/1520-0469(1988)045<0463:ATFSLL>2.0.CO;2.

Rowe, S. M., and M. H. Hitchman, 2015: On the role of inertial instability in stratosphere troposphere exchange near midlatitude cyclones. *J. Atmos. Sci.*, **72**, 2131–2151, https://doi.org/10.1175/JAS-D-14-0210.1.

——, and ——, 2016: On the relationship between inertial instability, poleward momentum surges, and jet intensifications near midlatitude cyclones. *J. Atmos. Sci.*, **73**, 2299–2315, https://doi.org/10.1175/JAS-D-15-0183.1.

——, and ——, 2020: Rapid destruction of a stratospheric potential vorticity anomaly by convectively induced inertial instability during the southern Wisconsin extreme flooding event of 20 August 2018. *Mon. Wea. Rev.*, **148**, 4397–4414, https://doi.org/10.1175/MWR-D-19-0213.1.

Seigel, R. B., and S. C. van den Heever, 2013: Squall-line intensification via hydrometeor recirculation. *J. Atmos. Sci.*, **70**, 2012–2031, https://doi.org/10.1175/JAS-D-12-0266.1.

Shige, S., and T. Satomura, 2000: The gravity wave response in the troposphere around deep convection. *J. Meteor. Soc. Japan*, **78**, 789–801, https://doi.org/10.2151/jmsj1965.78.6_789.

Smull, B. F., and R. A. Houze Jr., 1987: Rear inflow in squall lines with trailing stratiform precipitation. *Mon. Wea. Rev.*, **115**, 2869–2889, https://doi.org/10.1175/1520-0493(1987)115<2869:RIISLW>2.0.CO;2.

Snyder, C., D. J. Muraki, R. Plougonven, and F. Zhang, 2007: Inertia–gravity waves generated within a dipole vortex. *J. Atmos. Sci.*, **64**, 4417–4431, https://doi.org/10.1175/2007JAS2351.1.

——, R. Plougonven, and D. J. Muiraki, 2009: Mechanisms for spontaneous gravity wave generation within a dipole vortex. *J. Atmos. Sci.*, **66**, 3464–3478, https://doi.org/10.1175/2009JAS3147.1.

Tripoli, G. J., 1992a: A non-hydrostatic mesoscale model designed to simulate scale interaction. *Mon. Wea. Rev.*, **120**, 1342–1359, https://doi.org/10.1175/1520-0493(1992)120<1342:ANMMDT>2.0.CO;2.

——, 1992b: An explicit three-dimensional nonhydrostatic numerical simulation of a tropical cyclone. *Meteor. Atmos. Phys.*, **49**, 229–254, https://doi.org/10.1007/BF01025409.

——, and W. R. Cotton, 1982: The Colorado State University three-dimensional cloud/mesoscale model-1982, Part I: General theoretical framework and sensitivity experiments. *J. Rech. Atmos.*, **16**, 185–219.

Wakimoto, R. M., H. V. Murphey, C. A. Davis, and N. T. Atkins, 2006: High winds generated by bow echoes. Part II: The relationship between the mesovortices and damaging straight-line winds. *Mon. Wea. Rev.*, **134**, 2813–2829, https://doi.org/10.1175/MWR3216.1.

Wang, S., F. Zhang, and C. Snyder, 2009: Generation and propagation of inertia-gravity waves from vortex dipoles and jets. *J. Atmos. Sci.*, **66**, 1294–1314, https://doi.org/10.1175/2008JAS2830.1.

Weijenborg, C., J. M. Chagnon, P. Friederichs, S. L. Gray, and A. Hense, 2017: Coherent evolution of potential vorticity anomalies associated with deep moist convection. *Quart. J. Roy. Meteor. Soc.*, **143**, 1254–1267, https://doi.org/10.1002/qj.3000.

Weisman, M. L., 1992: The role of convectively generated rear-inflow jets in the evolution of long-lived mesoconvective systems. *J. Atmos. Sci.*, **49**, 1826–1847, https://doi.org/10.1175/1520-0469(1992)049<1826:TROCGR>2.0.CO;2.

——, 1993: The genesis of severe, long-lived bow echoes. *J. Atmos. Sci.*, **50**, 645–670, https://doi.org/10.1175/1520-0469(1993)050<0645:TGOSLL>2.0.CO;2.

——, and R. F. Trapp, 2003: Low-level mesovortices within squall lines and bow echoes. Part I: Overview and dependence on environmental shear. *Mon. Wea. Rev.*, **131**, 2779–2803, https://doi.org/10.1175/1520-0493(2003)131<2779:LMWSLA>2.0.CO;2.

——, and R. Rotunno, 2004: "A theory for strong long-lived squall lines" revisited. *J. Atmos. Sci.*, **61**, 361–382, https://doi.org/10.1175/1520-0469(2004)061<0361:ATFSLS>2.0.CO;2.

——, C. Evans, and L. Bosart, 2013: The 8 May 2009 superderecho: Analysis of a real-time explicit convective forecast. *Wea. Forecasting*, **28**, 863–892, https://doi.org/10.1175/WAF-D-12-00023.1.

Wernli, H., and H. C. Davies, 1997: A Lagrangian-based analysis of extratropical cyclones. I: The method and some applications. *Quart. J. Roy. Meteor. Soc.*, **123**, 467–489, https://doi.org/10.1002/qj.49712353811.

Xu, X., M. Xue, and Y. Wang, 2015: The genesis of mesovortices within a real-data simulation of a bow echo system. *J. Atmos. Sci.*, **72**, 1963–1986, https://doi.org/10.1175/JAS-D-14-0209.1.